Annual cycle of aerosol properties over the central Arctic during MOSAiC 2019-2020 — light-extinction, CCN, and INP levels from the boundary layer to the tropopause

Albert Ansmann[1], Kevin Ohneiser[1], Ronny Engelmann[1], Martin Radenz[1], Hannes Griesche[1], Julian Hofer[1], Dietrich Althausen[1], Jessie M. Creamean[2], Matthew C. Boyer[3], Daniel A. Knopf[4], Sandro Dahlke[5], Marion Maturilli[5], Henriette Gebauer[1], Johannes Bühl[1], Cristofer Jimenez[1], Patric Seifert[1], and Ulla Wandinger[1]

[1]Leibniz Institute for Tropospheric Research, Leipzig, Germany
[2]Department of Atmospheric Science, Colorado State University, Fort Collins, CO 80526, USA
[3]Institute for Atmospheric and Earth System Research /Physics, University of Helsinki, Helsinki, Finland
[4]School of Marine and Atmospheric Sciences, Stony Brook University, Stony Brook, NY 11794, USA
[5]Alfred Wegener Institute, Helmholtz Centre for Polar and Marine Research, Potsdam, Germany

Correspondence: A. Ansmann
(albert@tropos.de)

Abstract.

The MOSAiC (Multidisciplinary drifting Observatory for the Study of Arctic Climate) expedition was the largest Arctic field campaign ever conducted. MOSAiC offered the unique opportunity to monitor and characterize aerosols and clouds with high vertical resolution up to 30 km height at latitudes from 80°-90°N over an entire year (October 2019 to September 2020). Without a clear knowledge of the complex aerosol layering, vertical structures, and dominating aerosol types and their impact on cloud formation a full understanding of the meteorological processes in the Arctic and thus advanced climate change research is impossible. Widespread ground-based in-situ observations in the Arctic are insufficient to provide these required aerosol and cloud data. In this article, a summary of our MOSAiC observations of tropospheric aerosol profiles with a state-of-the-art multiwavelength polarization Raman lidar aboard the icebreaker Polarstern is presented. Particle optical properties, i.e., light-extinction profiles and aerosol optical thickness (AOT), and estimates of cloud-relevant aerosol properties (cloud condensation nucleus (CCN) and ice-nucleating particle (INP) number concentrations are discussed, separately for the lowest part of the troposphere (atmospheric boundary layer, ABL), within the lower free troposphere (around 2000 m height), and at cirrus level close to the tropopause. In situ observations of the particle number concentration and INPs aboard Polarstern are included in the study. A strong decrease in the aerosol amount with height in winter and moderate vertical variations in summer were observed in terms of the particle extinction coefficient. The 532 nm light-extinction values dropped from > 50 Mm^{-1} close to the surface to < 5 Mm^{-1} in 4-6 km height in the winter months. Lofted aged wildfire smoke layers caused a re-increase of the aerosol concentration towards the tropopause. In summer (June to August 2020), much lower particle extinction coefficients, frequently as low as 1-5 Mm^{-1}, were observed in the ABL. Aerosol removal, controlled by cloud scavenging processes (widely suppressed in winter, very efficient in summer) in the lowermost 1-2 km of the atmosphere, seem to be the

main reason for the strong differences between winter and summer aerosol conditions. A complete annual cycle of the AOT in the central Arctic could be measured. This is a valuable addition to the summer time observations with sun photometers of the Arctic Aerosol Robotic Network (AERONET). In line with the pronounced annual cycle in the aerosol optical properties, typical CCN number concentrations (0.2% supersaturation level) ranged from 50-500 cm^{-3} in winter to 10-100 cm^{-3} in summer in the ABL. In the lower free troposphere (at 2000 m), however, the CCN level was roughly constant throughout the year with values mostly from 30-100 cm^{-3}. A strong contrast between winter and summer was also given in terms of ABL INPs which control ice production in low-level clouds. While soil dust (from surrounding continents) is probably the main INP type during the autumn, winter and spring months, local sea spray aerosol (with a biogenic aerosol component) seems to dominate the ice nucleation in the ABL during the summer months (June-August). The strong winter-vs-summer contrast in the INP number concentration by roughly 2-3 orders of magnitude in the lower troposphere is however mainly caused by the strong cloud temperature contrast. An unique event of the MOSAiC expedition was the occurrence of a long-lasting wildfire smoke layer in the upper troposphere and lower stratosphere. Our observations suggest that the smoke particles frequently triggered cirrus formation close to the tropopause from October 2019 to May 2020.

1   Introduction

The Arctic, as part of the highly polluted northern hemisphere, can no longer be regarded as a pristine environment that is widely decoupled from the pollution centers of Asia, Europe, and North America (Abbatt et al., 2019; Willis et al., 2018, 2019; Schmale et al., 2021, 2022). The increasing number of extreme wildfires associated with long-distance transport of smoke towards all latitudes from the tropics to the North Pole is a new aspect that contributes in addition to strong changes in the environmental conditions in the Arctic (Xian et al., 2022a, b), even up to the stratosphere (Ohneiser et al., 2021; Ansmann et al., 2023). In order to consider these changes in climate modeling, especially in simulations of aerosol-cloud-precipitation inter- actions, an improved knowledge of the aerosol conditions as a function of height and season is required. However, vertically resolved observations of aerosol properties in the Arctic are scarce, and almost absent for the winter half year.

The MOSAiC (Multidisciplinary drifting Observatory for the Study of Arctic Climate) expedition offered the unique oppor- tunity to collect a dense data set of aerosol profiles in the North Pole region throughout a full year (Engelmann et al., 2021; Ohneiser et al., 2021). MOSAiC was the largest Arctic research initiative in history and took place from September 2019 to October 2020. Observations were mostly performed at latitudes $> 80°$N. The goal of the MOSAiC expedition was to take the closest look ever at the Arctic as the epicenter of global warming and to gain fundamental insights that are key to better understand global climate change. A rather detailed monitoring of the atmosphere, cryosphere and biosphere in the Central Arctic was realized (see the overview articles in the MOSAiC Special Issue in Elementa) (Elementa, 2022). The German ice- breaker Polarstern (Knust, 2017) served as the main MOSAiC platform for advanced active remote sensing of the atmosphere with several lidar and cloud radar instruments (Shupe et al., 2022). Polarstern was trapped in the ice and drifted through the Arctic Ocean from 4 October 2019 to 16 May 2020, however was then forced to leave the ice zone for logistical reasons in

the beginning of June and August 2020. The observations in ice at latitudes $> 85°$N could be continued from 21 August to 20 September 2020.

A state-of-the-art multiwavelength aerosol-cloud Raman lidar (Engelmann et al., 2016; Jimenez et al., 2020) aboard Polarstern was continuously operated side by side with the ARM (Atmospheric Radiation Measurement) mobile facility 1 (AMF-1) and collected tropospheric and stratospheric aerosol and cloud profile data throughout the expedition period. Our role in the MOSAiC consortium was to provide a seasonally resolved and height-resolved characterization of aerosols and clouds in the North Pole region from the surface up to 30 km height (Engelmann et al., 2021).

Ohneiser et al. (2021) focused on the lidar observations of the aerosol in the upper troposphere and lower stratosphere (UTLS). A lofted aerosol layer was continuously observed from about 5 to 20 km height for more than 7 months (October 2019 to mid-May 2020). The aerosol consisted of Siberian wildfire smoke in the lower part and Raikoke volcanic sulfate aerosol in the upper part of the UTLS aerosol layer (Ohneiser et al., 2021; Ansmann et al., 2023). In this article here, we present part 2 of our MOSAiC aerosol lidar observations aboard Polarstern and summarize our findings regarding the optical and cloud-relevant properties of tropospheric aerosols (from 0-10 km height) observed between 80° and 90°N during the MOSAiC year.

Let us briefly outline several gaps in our knowledge about Arctic aerosols with emphasizes on aerosol-cloud interaction and how the MOSAiC lidar and in situ observation aboard Polarstern may contribute to this field of atmospheric research. As stated by Shupe et al. (2022), a main MOSAiC science question is: What are the processes that regulate the formation, properties, precipitation, and lifetime of Arctic clouds and what is the impact of aerosols in these processes?

To answer this question, ground-based in situ aerosol characterization all over the Arctic (complemented by sporadic aircraft measurements during the spring and summer months) is of great value (see, e.g., Willis et al., 2018; Abbatt et al., 2019; Wex et al., 2019), however, clearly not sufficient. In terms of aerosol and ice nucleation conditions, at least three height regimes need to be distinguished: (1) The near-surface layer (atmospheric boundary layer, ABL) contains mainly local aerosol particles in summer (June to August), originating from marine sources (Creamean et al., 2018, 2019, 2022; Zeppenfeld et al., 2019; Wex et al., 2019; Hartmann et al., 2021; Alpert et al., 2022; Li et al., 2022; Sze et al., 2023; Carlsen and David, 2022), and Arctic haze, i.e., mixtures of aged anthropogenic particles, smoke, and desert and agricultural soil dust, in winter (see, e.g., Wang et al., 2011; Law et al., 2014; Willis et al., 2018; Abbatt et al., 2019; Engelmann et al., 2021). Because of biogenic substances of the summertime sea spray aerosol aerosol, ice nucleation can be initiated at likewise high temperatures of -5 to $-10°$C (Wex et al., 2019; Creamean et al., 2022; Alpert et al., 2022). Mineral dust particles, on the other hand, become ice active mainly at temperatures below -15 to $-20°$C (Ansmann et al., 2008; Kanji et al., 2017) and thus control ice nucleation in the winter-time ABL. Agricultural soil dust containing biological and biogenic material may already significantly trigger ice nucleation at temperatures of -10 to $-15°$C (Tobo et al., 2014; O'Sullivan et al., 2014).

(2) The second height regime is the lower to middle free troposphere (Griesche et al., 2021), decoupled from the ABL. This layer mostly contains long-range-transported continental aerosol disregarding the season of the year (Stohl, 2006; Zhao et al., 2022). Desert dust and agricultural soil dust are the main INP aerosol types (DeMott et al., 2015; Kanji et al., 2017). Recently, Tobo et al. (2019) pointed to the potential importance of dust from glacial sources containing biogenic material that may trigger ice nucleation at high temperatures above $-15°$C. This dust component may be present in the lower free

troposphere up to 2-3 km height during the summer months (Kawai et al., 2023). In the ABL and lower free troposphere, the majority of Arctic liquid-water and mixed-phased clouds develop (Carlsen and David, 2022). As was first found in tropical and subtropical mixed-phase clouds (Ansmann et al., 2008, 2009) and later confirmed for Arctic and mid latitude clouds (de Boer et al., 2011; Westbrook and Illingworth, 2011), immersion freezing, i.e., freezing of liquid-water droplets by nucleation of ice on an INP immersed in the droplets, is the dominating ice nucleation mode in the heterogeneous ice nucleation temperature regime ($> -38°C$), and thus in the lower Arctic troposphere.

(3) The third layer (cirrus regime) extends from about 5 km to the tropopause. UTLS sulfate background aerosol with traces of aged (parly coated) desert and agricultural soil dust as well as soot particles may dominate here (Martinsson et al., 2019; Brock et al., 2021). Wildfire smoke increasingly contributes to the aerosol burden in the Arctic troposphere during the last years (Xian et al., 2022a, b). Smoke particles dominated at heights above 6-7 km from October 2019 to May 2020 over the Polarstern and had a strong impact on cirrus formation as will be discussed in Sect. 5.3 and more extensively in a follow-up paper.

This article is organized as follows. In Sects. 2 and 3, the applied instrumentation and lidar data analysis methods are described, respectively. Several case studies of tropospheric aerosol profiling (covering the full range of aerosol conditions from rather clean to polluted) in summer are discussed in Sect. 4.1. Case studies for the winter half year during the Arctic haze period were presented already by Engelmann et al. (2021). The annual cycle of tropospheric aerosol profiles and aerosol optical thickness (AOT) observed during the MOSAiC year 2019-2020 are then discussed in Sects. 4.2 and 4.3. Time series of in-situ-measured and lidar-derived particle number concentration, used as proxy for the cloud condensation nucleus (CCN) number concentration, and of the ice-nucleating particle (INP) number concentration for the height levels of 250 m (near ABL top), 2000 m (free troposphere), and in the upper troposphere are presented in Sect. 5. A short summary and concluding remarks complete the study in Sect. 6.

2 MOSAiC instrumentation

2.1 MOSAiC Polarstern route

The full track of the Polarstern is given in Creamean et al. (2022), Shupe et al. (2022), and Boyer et al. (2023). The ice breaker drifted with the ice through the central Arctic at latitudes $\geq 85°N$ until the beginning of April and cruised between 83-84°N until 22 May 2020 (Engelmann et al., 2021). Because of the COVID-19 pandemic Polarstern had to leave the ice zone and to transit to Ny-Ålesund (78.9°N, 11.9°E) on the island of Spitsbergen in Svalbard, Norway, in the beginning of June 2020 to exchange science team members. The same procedure was necessary in the beginning of August 2020. As a consequence of theses complications, from June to mid of August 2020, the observations were restricted to latitudes of 80°-82°N. From mid August to the end of September 2020, observations were again taken at latitudes $\geq$85°N.

2.2 MOSAiC Polarstern lidar Polly

The remote sensing infrastructure aboard Polarstern was discussed in Engelmann et al. (2021). The multiwavelength polarization Raman lidar Polly (POrtabLe Lidar sYstem) (Engelmann et al., 2016) performed continuous measurements from 26 September 2019 to 2 October 2020 (Polly, 2022). A detailed description of the Polly instrument with all the upgrades realized during the last years can be found in Hofer et al. (2017) and Jimenez et al. (2020). The lidar is mounted inside the OCEANET-Atmosphere container of the Leibniz Institute for Tropospheric Research (TROPOS). This container is designed for routine operation aboard Polarstern between Bremerhaven, Germany, and Cape Town, South Africa, and for cruises from Bremerhaven to Punta Arenas, Chile (Kanitz et al., 2011, 2013; Bohlmann et al., 2018; Yin et al., 2019), and participated in an Arctic field campaign in June and July 2017 for the first time (Griesche et al., 2020, 2021).

An overview of all measured and derived lidar products is given in Table 1 in Engelmann et al. (2021). The retrieval of the microphysical and cloud-relevant aerosol properties in Table 1 (in this article) are presented in Sects. 3.1-3.4. The basic aerosol observations comprise height profiles of the particle backscatter coefficient at 355, 532, and 1064 nm, the particle extinction coefficient at 355 and 532 nm, the respective extinction-to-backscatter ratio (lidar ratio) at 355 and 532 nm, and the particle linear polarization ratio at 355 and 532 nm (Baars et al., 2016; Hofer et al., 2017; Ohneiser et al., 2021). Lidar signals are measured with a near-range and a far-range telescope, covering different height ranges so that backscatter coefficients and depolarization ratios are measurable from about 100 m to 30 km, and extinction coefficients and lidar ratios from about 400 m upward. The main features of the basic MOSAiC aerosol data analysis (including signal correction, Rayleigh backscattering and extinction correction, temporal averaging and vertical smoothing of signal profiles) are described in Ohneiser et al. (2020, 2021, 2022). The retrieval scheme applied to obtain the aerosol properties from the lidar observations that are relevant in the studies of aerosol-cloud interaction are outlined in Sect. 3.

2.3 MICROTOPS II sunphotometer

A handheld MICROTOPS II sunphotometer (Ichoku et al., 2002) was used by the TROPOS lidar team aboard Polarstern to measure the AOT at 440, 500, 870, and 1020 nm wavelength whenever possible to support lidar observations of particle extinction profiles. Unfortunately, this photometer was available aboard Polarstern from June to September 2020, only. The MOSAiC sun and lunar photometer installed by the TROPOS team in September 2019 aboard Polarstern failed to work properly. MICROTOPS II is the standard device of MAN (Maritime Aerosol Network) (Smirnov et al., 2009) which is a component of AERONET (Holben et al., 1998). An operator is required to point the photometer to the Sun for a while to take stable measurements. Continuous, unattended measurements are not possible. The data are stored in the MAN (Maritime Aerosol Network) data base (AERONET-MAN, 2022).

2.4 CALIOP

To check the representativeness of the one-year MOSAiC aerosol observations, we compared our findings with Cloud-Aerosol Lidar with Orthogonal Polarization (CALIOP) observations (Winker et al., 2009, 2010). The spaceborne lidar CALIOP mon-

itored Arctic aerosol profiles throughout the year (even during the winter months) from June 2006 to August 2023. These observations are favorable for comparison, despite the fact that the maximum latitude covered by the CALIOP observations is 81.8°N and MOSAiC measurements were performed from 80°-90°N. Yang et al. (2021) analyzed all Arctic CALIOP aerosol profiles for latitudes from 65°-82°N from June 2006 to December 2019 and present time series of monthly resolved 13-14-year mean AOT and seasonally resolved 14-year mean summer and 13-year mean winter height profiles of the particle extinction coefficient at 532 nm.

2.5 Instrumentation for in situ measurements of aerosol microphysical properties and INP number concentrations aboard Polarstern

Continuous in situ observations of dry particle number concentrations, particle number size distributions and black carbon mass concentrations (Boyer et al., 2023) as well as of INP number concentrations (Creamean et al., 2022) were performed aboard Polarstern during the entire MOSAiC period from October 2019 to September 2020.

A commercial Scanning Mobility Particle Sizer (SMPS) was used to measure the particle number size distribution (PNSD). The instrumental setup includes a condensation particle counter. The particle number concentration was calculated by integrating over the PNSD, which was evaluated in three size (diameter) categories in this study: 10–25 nm (nucleation mode), 25–100 nm (Aitken mode), and 100–500 nm (accumulation mode). The SMPS was installed in the Aerosol Observing System (AOS) container that was operated as part of the United States Department of Energy Atmospheric Radiation Measurement (ARM) user facility aboard Polarstern. The AOS was equipped with a total aerosol inlet that was 5 m in length, which corresponds to an inlet height of approximately 18m above the sea surface (Boyer et al., 2023).

The number concentrations $n_{50,\mathrm{dry}}$, discussed in Sect. 5.1, considers dried particles with diameters from 100 to 500 nm. $n_{50,\mathrm{dry}}$ is used as proxy for the CCN number concentration n_{CCN} for the water supersaturation value of 0.2%. CCN concentrations were also measured aboard Polarstern (Dada et al., 2022) and will be included in the discussions of the MOSAiC observations in Sect. 5.1. The in situ observations of $n_{50,\mathrm{dry}}$ were carefully checked and corrected for contamination by local pollution (exhaust plume of Polarstern and further aerosol sources on the near-by measurement field station on the pack ice) (Beck et al., 2022). About 40% of the measured data had to be removed (Boyer et al., 2023).

Regarding the INP observations, aerosol particles were collected in four size ranges by using the Colorado State University (CSU) 4-stage Davis Rotating-drum Unit for Monitoring cascading impactor (DRUM) through the AOS inlet (Creamean et al., 2022). The DRUM collected daily integrated samples from 0.15 to > 12 μm (particle diameter). The AOS inlet has a high transmission efficiency for particles from 10 nm to 4 μm but has large uncertainties in transmission efficiency above 4 μm due to low ambient aerosol signal in that size range. Daily mean INP samples, considering aerosol particles from 10 nm to 4 μm, are thus discussed in Sect. 5.2. The INP number concentration (immersion freezing mode, i.e., ice nucleation initiated by INPs immersed in water droplets) was determined by applying the CSU cold plate method to the 24 h aerosol samples.

2.6 Air mass source analysis

Ensemble backward trajectories were computed (as part of the case studies) in Sect. 4.1 by using the NOAA (National Oceanic and Atmospheric Administration) HYSPLIT (HYbrid Single-Particle Lagrangian Integrated Trajectory) model (HYSPLIT, 2022; Stein et al., 2015; Rolph et al., 2017). The arrival heights were set into observed aerosol layers to identify the origin of the pollution. Furthermore, the aerosol-source attribution method of Radenz et al. (2021) was applied. This air mass identification tool was developed to support the interpretation and evaluation of lidar profiles. We computed the normalized (accumulated) residence time, during which the air masses traveled within the well-mixed boundary layer at heights below 2 km, before they crossed Polarstern at well specified arrival heights (from the surface to 12 km with a resolution of 500 m). This analysis is also based on HYSPLIT backward trajectories. 10 d backward trajectory analysis was found to be sufficient to identify the continental pollution sources (Asia, Europe, or North America), or, in cases with background aerosol conditions that the respective air masses obviously did not cross any populated continental region (aerosol source region) during a period longer than a week before arrival over Polarstern.

3 Lidar retrieval of microphysical aerosol properties, CCN, and INP number concentrations: The POLIPHON method

During the last 10 years, we developed a complex lidar retrieval scheme to obtain information about microphysical and cloud-relevant parameters from lidar backscatter and extinction profiles for a number of different aerosol types (Mamouri and Ansmann, 2016, 2017; Ansmann et al., 2019a, 2021). In this section, we expand the methodology towards Arctic aerosol conditions.

3.1 Arctic aerosol model: optical vs microphysical properties

The POLIPHON (Polarization Lidar Photometer Networking) method is a robust and practicable single-wavelength lidar method to derive number, surface area, and volume concentrations of particles from the measured optical properties in the troposphere and stratosphere and to estimate tropospheric CCN and INP number concentrations. The POLIPHON method makes use of the height profiles of the 532 nm particle backscatter coefficient and particle depolarization ratio and converts the measured backscatter into microphysical properties by using aerosol-type-dependent conversion factors. These conversion factors are derived from long-term AERONET (Aerosol Robotic Network) observations (Holben et al., 1998) around the globe and connect the optical and underlying microphysical properties for main atmospheric aerosol components, such as desert dust, marine particles, anthropogenic haze, and wildfire smoke.

In the framework of the MOSAiC data analysis, Arctic AERONET observations were used to derive a respective set of conversion factors for Arctic aerosol particles, i.e., a mixture of aged anthropogenic haze, biomass burning smoke, and soil dust after long-distance transport and a minor contribution of marine particles. Sun and sky photometer observations of 11 Arctic AERONET stations covering up to almost 25 years of observations (1997-2021) were considered in this approach (AERONET, 2022). According to these Arctic AERONET observations, the Arctic aerosol shows remarkably constant properties from the

spring season to the late summer season. Typical Ångström exponents (for the 440-870 nm spectral range) are 1.4-1.6, clearly indicating non-marine, fine-mode aerosol components. The fine-mode fraction is around 0.9 and indicates the dominance of anthropogenic pollution and biomass-burning smoke. Most of the time the AOT is found in the range of 0.015-0.15 at 500 nm which is in good agreement with the studies of Tomasi et al. (2012, 2015) and Xian et al. (2022a).

215   To obtain height profiles of Arctic aerosols in terms of standard products such as volume concentration $v(z)$, surface area concentration $s(z)$, and particle number concentrations $n_{\mathrm{rmin}}(z)$ considering all particles with radius > rmin, the following basic relationships are available:

$$v(z) = c_{\mathrm{v}} L \beta(z) \,, \tag{1}$$

$$s(z) = c_{\mathrm{s}} L \beta(z) \,, \tag{2}$$

220    $$n_{\mathrm{rmin}}(z) = c_{\mathrm{rmin}} L \beta(z) \tag{3}$$

with the particle backscatter coefficient $\beta(z)$ at height z and the extinction-to-backscatter or lidar ratio L. Arctic tropospheric lidar ratios were observed in the range from 20–90 sr at 532 nm (Ritter et al., 2016; Engelmann et al., 2021) and accumulated between 40 and 70 sr. All conversion factors, i.e., the extinction-to-volume conversion factor c_{v}, the extinction-to-surface-area conversion factor c_{s}, and the extinction-to-number conversion factors c_{rmin} for 532 nm in Eqs. 1 - 3) are obtained from the

225   analysis of the Arctic AERONET observations regarding the relationship between measured aerosol optical properties (500 or 532 nm AOT) and AERONET retrieval products (column values of n_{rmin}, s, and v). Details of the determination of the conversion factors can be found in Mamouri and Ansmann (2016, 2017). Table 2 shows the obtained conversion factors for Arctic aerosols. These quantities are partly used as input in the estimation of CCN and INP number concentrations as explained in Sects. 3.3 and 3.4. In the MOSAiC data analysis, we applied the Arctic conversion factors to all MOSAiC lidar observations

230   at the selected height levels of 250 m and 2000 m, discussed in Sects. 5.1 and 5.2. Since, the conversion factors were derived for summer time aerosol conditions they may not be fully applicable to Arctic haze observations during the winter half year. This aspect is further discussed in Sects. 3.3, 3.4.1, and 5.1.

Input in these CCN and INP retrieval procedures are aerosol parameters for dry conditions. However, AERONET sunphotometer observations in the Arctic are typically performed at RH around 80% in the lower, aerosol-laden atmosphere according

235   to the MOSAiC 2019-2020 radiosonde observations (Maturilli et al., 2021) and the study of Shupe et al. (2011) at Arctic land-based observatories. So, all the conversion factors are derived for aerosol scenarios observed at high humidity.

The aerosol particles contain a considerable amount of water at high humidity so that the aerosol backscatter and extinction coefficients are significantly enhanced compared to respective optical properties for dry conditions. To obtain the dry aerosol parameters (e.g., $n_{50,\mathrm{dry}}$ needed in the CCN estimation, s_{dry} needed in the INP retrieval) the following procedure was necessary

240   to correct for water uptake effects: We make use of the well-known so-called enhancement factor $(1 - \mathrm{RH}/100\%)^{\gamma}$ with RH in % and an exponent γ of, e.g., -0.46 for continental fine-mode particles (see, e.g., Skupin et al., 2016). The enhancement factor relates the optical properties of the particles measured at ambient RH conditions (e.g., at 80%) to respective values for dry conditions (e.g., RH of 0-20%). In the first step, we converted the lidar profiles of the particle extinction coefficient for ambient RH (known from the MOSAiC radiosonde RH profiles) to values for RH=80% by multiplying the measured extinction values

245 with the factor $(1-80/100\%)^{-0.46}/(1-\mathrm{RH}/100\%)^{-0.46}$. Then, we multiplied these extinction coefficients for RH=80% with the conversion factor of c_{85} to obtain an estimate for the height profile of the particle number concentration $n_{85}(z)$ at RH=80%. This number concentration n_{85} (considering all particles with ambient radius >85 nm) was then interpreted as an appropriate proxy of $n_{50,\mathrm{dry}}$. It is assumed here, that water uptake causes an increase of the radius of dry particles by roughly a factor of 1.5 when RH is increased from low RH to high RH values around 80% so that particles with radius >80-85 nm will shrink to

250 particles with radius >50 nm when RH is reduced from 80% to less than 30-40%.

In order to obtain the height profile of the particle surface area concentration $s_{\mathrm{dry}}(z)$ for Arctic aerosols, we used the computed lidar extinction profiles for RH=80% and multiplied these profiles with the conversion factor c_{s} to obtain the surface-area profile $s(z)$ for RH=80%. Then we converted this s profile to a profile for RH=20% by multiplying all s values with the factor $(1-20/100\%)^{-0.46}/(1-80/100\%)^{-0.46}$. This profile, after water uptake correction, was interpreted as s_{dry}.

255 According to Table 1, the microphysical aerosol properties (dry volume and surface-area concentrations) can be estimated with an uncertainty of 25%. The uncertainty is of the order of 50% in the case of the $n_{50,\mathrm{dry}}$ retrieval when the aerosol type is well known as comparisons with airborne in situ measurements of CCN number concentrations showed (Düsing et al., 2018; Choudhury et al., 2022). The uncertainty is larger (within a factor of 2) when the aerosol type and thus the aerosol size distribution for this aerosol type) is not well known or when a rather complex mixture of different hygroscopic and hydrophobic,

260 fine and coarse aerosol particles prevail (Haarig et al., 2019; Georgoulias et al., 2020).

3.2 Upper tropospheric aerosol conversion factors

In Sect. 5.3, we present INP time series for wildfire smoke particles at cirrus level (October 2019 to May 2020 and September 2020) and for mineral dust (June-August 2020). In the respective lidar data analysis following Eq. (2), we use the extinction-to-surface area conversion factor c_{s} of 1.75×10^{-12} Mm m^2 cm^{-3} for aged UTLS wildfire smoke and a characteristic lidar

265 ratio of 85 sr at 532 nm in the particle surface-area retrieval (Ansmann et al., 2021; Ohneiser et al., 2021). We converted the optical properties measured at upper tropospheric humidity conditions to values for RH=20% in a first step and multiplied the RH-corrected extinction values with the smoke-related conversion factor to obtain s_{dry} for smoke conditions. The wildfire conversion factors were applied to all near-tropopause MOSAiC observations in the autumn, winter, and spring seasons of 2019-2020.

270 In a similar way, the extinction-to-surface-area conversion factor for aged continental aerosol of $c_{\mathrm{s}} = 2.8 \times 10^{-12}$ Mm m^2 cm^{-3} (Mamouri and Ansmann, 2016) was applied for the summer months (June-August) and we assumed a lidar ratio of 55 sr for these continental particles. Furthermore, we assumed that aged desert (clay) dust particles were exclusively responsible for ice nucleation in the upper troposphere during the summer months. The estimated dust fraction multiplied with the total particle surface area s_{dry} was then used as aerosol input in the INP retrieval. More details are given in Sects. 3.4.1, 3.4.2,

275 and 5.3.

From the methodological point of view the most correct way to determined the dust-related surface area s_{dry} would be to use the measured particle linear depolarization ratio and to separate dust and non-dust components to the backscatter and extinction coefficients in the first step, and to apply the dust conversion factor to the dust-related extinction coefficients to obtain the dust

s_dry values in the second step (Mamouri and Ansmann, 2016). However, such an approach is only possible if the dust fraction
280 is >10% (and thus clearly detectable in the depolarization measurements) and not <5% as was the case during the MOSAiC expedition.

3.3   Estimation of CCN number concentration

In Sect. 5.1, lidar-derived time series of the CCN number concentration n_CCN at 250 and 2000 m height are discussed. CCN values at 250 m height may well represent the aerosol conditions during low level cloud formation at the top of the Arctic
285 ABL. According to Peng et al. (2023), the ABL top height was mostly between 100 and 400 m height over Polarstern during the MOSAiC year. Time series at 2000 m height provide insight into the CCN conditions in the lower free troposphere where stratiform mixed-phase cloud layers frequently develop.

As discussed in Mamouri and Ansmann (2016), the particle number concentration $n_\text{50,dry}$ can be used as proxy for n_CCN in an air parcel in which the relative humidity over water is 100.2% (supersaturation level of 0.2%, $S_\text{WAT} = 1.002$):

$$n_\text{CCN}(S_\text{WAT}) = f_\text{ss} \times n_\text{50,dry}. \tag{4}$$

The factor f_ss is set to 1.0 for a water supersaturation value of 0.2% and is introduced to estimate CCN number concentrations for lower and higher supersaturation levels. Values for f_ss were found to be about 0.4, 1.5, and 2.0 for $S_\text{WAT} = 1.001$, 1.004, and 1.007, respectively, in the Canadian Arctic (Tuktoyaktuk, 69.4°N, 133.0°W) in the spring of 2014 (Herenz et al., 2018). According to their observations the critical diameter d_crit was 107 nm at $S_\text{WAT} = 1.002$. For the critical diameter d_crit, the
295 integral over the independently measured particle size distribution from d_crit to the maximum size bin, d_max, is equal to the measured CCN number concentration n_CCN. d_crit decreases with increasing supersaturation. Also Dada et al. (2022) derived a critical diameter around 100 nm for a supersaturation of 0.2% from MOSAiC observation aboard Polarstern during a warm airmass intrusion event in April 2020. All these findings corroborate that $n_\text{50,dry}$ is an appropriate proxy for n_CCN for the supersaturation level of 0.2%.

300 As mentioned in Sect. 3.1, we used the Arctic conversion factors obtained from summer time AERONET observations in the analysis of the entire MOSAiC lidar data (measured at 250 and 2000 m height). However, especially the conversion factor c_85 (and also c_65) in Table 2, used in the n_50 and CCN retrieval, are very sensitive to size distribution details of the given aerosol conditions, and thus may no hold at all for winter time (Arctic haze) conditions. This potential uncertainty source is discussed in Sect. 5.1, when we compare the lidar estimates of $n_\text{50,dry}$ with in-situ measured $n_\text{50,dry}$ values.

305 ## 3.4   Estimation of INP number concentration

In Sects. 5.2 and in Sect. 5.3, we present MOSAiC time series of lidar-derived INP estimates for the height levels of 250 m and 2000 m above Polarstern, and for the height 1 km below the tropopause. INP time series for 250 and 2000 m height indicate the immersion freezing conditions in mixed-phase clouds in the ABL and lower free troposphere, and the INP number concentration values for the uppermost troposphere indicate the potential of aerosol particles to influence ice nucleation at
310 cirrus level. As outlined in the introduction, the dominating ice-nucleating aerosol type in the ABL is probably desert and

agricultural soil dust in winter. Sea spray aerosol (SSA), carrying ice-active substances of biogenic origin, is assumed to control ice nucleation in the summer ABL. In the lower free troposphere (at 2000 m height in this study), we assume that clay mineral dust is the only INP type throughout the year. In the upper troposphere, we assume smoke and dust particles serve as INPs in the deposition ice nucleation (DIN) mode. In Sect. 3.4.1, we describe the immersion freezing INP parameterization for clay mineral dust and SSA particles, and in Sect. 3.4.2, the DIN parameterization for smoke and clay mineral dust particles for upper tropospheric ice nucleation conditions. Thus, we ignore in our study a contribution by dust from agricultural and glacial sources.

3.4.1 INP parameterization (immersion freezing)

Zhao et al. (2022) recently discussed the long-range transport of desert dust from Asia to the Arctic and showed that a few percent of dust must be expected everywhere over the Arctic in the tropospheric column from the surface up to the tropopause. The studies of Yang et al. (2021) and Xian et al. (2022a) support this finding. The only exception may be the ABL during the summer months. During long-distance travel from the main dust sources, the dust particles probably get significantly contaminated with substances that reduce their ice nucleation efficiency. As pointed out in the review article of Willis et al. (2018), aerosol particles can undergo significant chemical aging and cloud processing along the transport path to Arctic regions. Aged dust particles may be partly or even completely coated with sulfate, nitrate, and organic substances. The potential to serve as INP may then be considerably reduced by an order of magnitude (Möhler et al., 2008; Cziczo et al., 2009; Wex et al., 2014; Augustin-Bauditz et al., 2014; Kulkarni et al., 2014; Kanji et al., 2017, 2019; Knopf et al., 2018).

The water-activity-based immersion freezing model ABIFM (Knopf and Alpert, 2013, 2023), drawn from the water-activity-based homogeneous ice nucleation theory (Koop et al., 2000), is used to estimate the INP number concentration n_{INP} in the lower troposphere (immersion freezing regime):

$$n_{\mathrm{INP}} = a_{\mathrm{frac}} s_{\mathrm{dry}} J_{\mathrm{het,IF}}(k, b, T, S_{\mathrm{ICE}}) f_{\mathrm{age}} \Delta t \tag{5}$$

with the contribution a_{frac} of the INP type of interest (dust or SSA) to the total particle surface area concentration s_{dry}, the ice-nucleation rate coefficient for immersion freezing $J_{\mathrm{het,IF}}$, which is computed as a function of aerosol-type-specific parameters k and b (see Knopf and Alpert, 2013; Alpert and Knopf, 2016; Alpert et al., 2022, for more details), ice-nucleation temperature T, and ice supersaturation S_{ICE}. In the case of dust particles, we used $k = 53.32$ and $b = -8.61$ in the computation of $J_{\mathrm{het,IF}}$ (Alpert and Knopf, 2016). These parameters follow from laboatoy studies with kaolinite particles (Wex et al., 2014). Kaolinite is a clay mineral. The values are $k = 26.6132$ and $b = -3.9346$ in the SSA-related calculation of $J_{\mathrm{het,IF}}$ (Alpert et al., 2022). The decrease of the ice nucleation efficiency of aged and contaminated dust particles is considered by the factor f_{age} set to 0.2 (Augustin-Bauditz et al., 2014; Wex et al., 2014). Ice nucleation (i.e., activation of INPs) takes place during the time interval Δt. The activation time for ice formation according to Eq. (5) is set to $\Delta t = 60$ s (as in Alpert et al., 2022) to be close to the time scales applied in the filter-based offline INP measurements (DeMott et al., 2016; Creamean et al., 2022).

As outlined in Sect 3.1, the surface area concentration s_{dry} is obtained from the conversion of the lidar extinction coefficients. We used the Arctic conversion factor c_s in Table 2 to estimated s_{dry} for heights below 3-4 km. In contrast to c_{65} and c_{85}, the

factors c_s and c_v are robust conversion factors and do not vary much from aerosol type to aerosol type, as long as the aerosol conditions are dominated by fine-mode aerosol, as it was the case for the selected height levels of 250 and 2000 m. According to our MOSAiC lidar observations, the dust fraction was always $a_{frac} \leq 0.05$. For SSA and smoke particles, a_{frac} was set to 1.0 in the respective INP retrievals in the ABL (SSA) and in the upper troposphere (smoke, described in the next section).

3.4.2 INP parameterization (deposition ice nucleation)

Very limited information about the INP conditions in the Arctic upper troposphere is available in the literature. A short review of field studies regarding aerosol-cirrus interaction is given in Sect. 5.3. During MOSAiC, wildfire smoke particles dominated over the central Arctic from October 2019 to May 2020 (Ohneiser et al., 2021) and also in September 2020. The ice nucleation efficiency of aged smoke particles is determined by organic material (organic carbon, OC). The black carbon (BC) or soot content is typically 2-3% (Dahlkötter et al., 2014; Yu et al., 2019; Torres et al., 2020; Ohneiser et al., 2023) and has no relevant impact on the ice-nucleating efficiency of aged wildfire smoke particles. Biomass-burning particles also contain humic-like substances which represent large macromolecules that could serve as INP at low temperatures of -50 to $-70°C$ (Wang and Knopf, 2011; Wang et al., 2012; Knopf et al., 2018).

Because of the complex chemical, microphysical, and morphological properties of aged fire smoke particles, which can occur as glassy, semi-liquid, and liquid aerosol particles, the development of smoke INP parameterization schemes is a crucial task (Knopf et al., 2018). The particles and released vapors in biomass burning plumes undergo chemical and physical aging processes on their way up to the tropopause and during long-range transport over weeks and months. Aging includes photochemical processes, heterogeneous chemical reactions on and in the particles, condensation of gases on the particle surfaces, collision and coagulation, and cloud processing (when acting as CCN or INPs in several consecutive cloud evolution and dissipation events). All these impacts change the chemical composition of the smoke particles, their morphological characteristics (size, shape, and internal structure), and the internal mixing state of the smoke particles.

In this exercise, we assume that smoke particles, after finalizing the aging process, show a core-shell structure with a BC-containing core and an OC-rich shell (OC for organic carbon), and that the ability to serve as INP mainly depends on the material in the shell and thus on the organic material of the particles. If the particles are in a glassy state, they can act as INPs in deposition ice nucleation (DIN) processes (Murray et al., 2010; Wang and Knopf, 2011; Wang et al., 2012). DIN is defined as ice formation occurring on the INP surface by water vapor deposition from the supersaturated gas phase. When the smoke particles can take up water and a liquid surface around the particles develops, immersion freezing can proceed (Wang et al., 2012; Knopf and Alpert, 2013; Knopf et al., 2018).

Goal of the MOSAiC aerosol study here is to demonstrate that the dust and smoke aerosols levels were high enough in the upper troposphere to trigger heterogeneous ice nucleation and to significantly influence cirrus formation. As we will discuss below, ice cyrstal number concentrations, retrieved from MOSAiC lidar and radar observations, are mostly in the range from 0.1 to 10 L^{-1} and thus point to the dominance of heterogeneous ice formation at cirrus level. Ice nucleation is initiated by lofting of air parcels during the updraft period of a gravity wave (Haag and Kärcher, 2004; Spichtinger et al., 2005; Kärcher et al., 2006; Kärcher and Podglajen, 2019). Gravity waves show time periods of typically 15-20 minutes (Kalesse and Kollias,

2013) and updraft phases of about 5 minutes (first quarter of the full temporal length) with updraft velocities ranging mostly from 10-50 cm s^{-1} (Barahona et al., 2019; Kärcher and Podglajen, 2019).

380   As mentioned, we assume that the aerosol in the upper troposphere consisted of wildfire smoke during the MOSAiC autumn, winter, and spring months. From June-August 2020, in the absence of pronounced wildfire smoke layers, the upper tropospheric aerosol was assumed to be an aerosol mixture mainly composed of anthropogenic haze, soil dust, and a small fraction of biomass burning smoke. We assume in our INP estimation that kaolinite particles dominate heterogeneous ice nucleation in the upper troposphere at -50° to-70°C under these aerosol mixture conditions.

385   We considered DIN as the main heterogeneous ice nucleation mode. The INP number concentration can be estimated by using the parameterization of Wang and Knopf (2011):

$$n_{\mathrm{INP}} = a_{\mathrm{frac}} s_{\mathrm{dry}} J_{\mathrm{het,DIN}}(c_{\mathrm{angle}}, T, S_{\mathrm{ICE}}) f_{\mathrm{age}} \Delta t. \tag{6}$$

The ice nucleation rate coefficient $J_{\mathrm{het,DIN}}$ is a function of the contact angle c_{angle}, ice-nucleation temperature T and ice supersaturation S_{ICE}. The selected contact angles are 12° and 26.5° for clay mineral dust and wildfire smoke INP computation,

390 respectively (Wang and Knopf, 2011). Though, for each species c_{angle} can range about 7°-10°. For these contact angles (12° and 26.5°), the ice nucleation onset RH$_{\mathrm{ICE,on}}$ is 107% (kaolinite) and 140.5% (smoke) (Wang and Knopf, 2011). In the case of dust, we set a_{frac} to 0.05 and f_{age} to 0.2 in Eq. (6) and $a_{\mathrm{frac}} = 1.0$ and $f_{\mathrm{age}} = 1.0$ in the case of wildfire smoke. The determination of s_{dry} for dust and smoke particles was outlined in the Sect. 3.2. Regarding the organic material, leonardite is selected (a standard humic acid surrogate material) to represent the amorphous organic coating of smoke particles. Leonardite,

395 an oxidation product of lignite, is a humic-acid-containing soft waxy particle (mineraloid), black or brown in color, and soluble in alkaline solutions. The INP characteristics of leonardite were studied in detail in laboratory experiments (Knopf and Alpert, 2013; Rigg et al., 2013).

     We simulated a gravity-wave-induced ascent of an air parcel to provide realistic numbers on ice nucleation events and related INP number concentrations. During the updraft phase, the temperature T decreases and S_{ICE} increases in the lofted air parcels

400 and ice nucleation starts when RH$_{\mathrm{ICE}}$ exceeds RH$_{\mathrm{ICE,on}}$. We set the mean updraft speed to 30 cm s^{-1} (mean value for the first quarter of the gravity wave period) and accumulated the INP number concentration for an ascent period of $\Delta t = 35$ s in the case of the very ice active dust particles and 88 s in the case of the much less ice active smoke particles. After 35 s (dust) and 88 s (smoke) of lofting, RH$_{\mathrm{ICE}}$ was 2% (dust) and about 6% (smoke) larger than RH$_{\mathrm{ICE,on}}$. We arbitrarily terminated the INP computation when the INP concentration reached 30 L^{-1} for a given smoke particle surface area concentration of

405 25 μm^2 cm^{-3}, following Eq. (6). In a similar way, we terminated the dust INP computation when the INP concentration reached 30 L^{-1} for a given total particle surface area concentration of 25 μm^2 cm^{-3} and by taking a dust fraction a_{frac} of 5% and an aging factor $f_{\mathrm{age}} = 0.2$ in Eq. (6) into account. We terminated the computation after 35 and 88 s assuming that water vapor deposition on the rapidly growing, freshly formed ice crystals reduces S_{ICE} considerably so that further nucleation is widely suppressed. This simplified approach is sufficient to provide an estimation of how many INPs were typically available

410 for ice nucleation in the upper troposphere over the high Arctic during the MOSAiC year. More information to the gravity wave simulations can be found in Mamouri et al. (2023) and in Sect. 5.3.

As indicated in Table 1, the uncertainty in the lidar-based estimation of the INP number concentration is large (an order magnitude). To validate the reliability of the INP retrieval procedures we make use of so-called closure studies in which the lidar-derived INP number concentrations (n_{INP}) are compared with estimated ice crystal number concentrations (n_{ICE}) from

415   lidar-radar observations in ice crystal virga (Ansmann et al., 2019b; Marinou et al., 2019; Engelmann et al., 2021). In this comparison, we assume that the number of ice cyrstals indicates the number of INPs ($n_{ICE} = n_{INP}$). Good agreement in these closure studies, i.e., similar estimates of n_{INP} and n_{ICE}, in the absence of secondary ice production (Ramelli et al., 2021), would indicate a high reliability of the selected INP parameterization. This closure concept will be applied in an extended MOSAiC study of mixed-phase and ice cloud systems (to be presented in follow-up articles).

420   ## 4 Observations, part 1: Aerosol layering and aerosol optical properties

Part 1 of the result sections 4 and 5 deals with the optical properties of Arctic aerosols observed during the MOSAiC Polarstern cruise. We start with four case studies in Sect. 4.1, before we present overviews and time series in Sects. 4.2 and 4.3.

4.1 Clean and polluted conditions during the MOSAiC summer: case studies

The three observations in Fig. 1 are selected because they cover the full range of MOSAiC summer scenarios from clean to
425   polluted conditions. As mentioned, winter time (Arctic haze) scenarios were discussed by Engelmann et al. (2021). On all three days, the lowest part of the troposphere was rather clean. Particle backscatter coefficients from 0.02-0.1 $Mm^{-1}sr^{-1}$ at 532 nm in Fig. 1a indicate particle extinction coefficients of about 1-6 Mm^{-1} (for a typical extinction-to-backscatter ratio of 50-60 sr). On 30 June 2020, Arctic background conditions were observed over the Polarstern with extinction coefficients < 5 Mm^{-1} throughout the entire troposphere. The backscatter peak at the surface was probably caused by weak fog which drifted over
430   the lidar during the signal averaging period (18-24 UTC). The lidar-derived 532 nm AOT was 0.023 on 30 June 2020 (when ignoring the fog-related near-surface backscatter peak). The MICROTOPS photometer measured a 500 nm AOT of 0.035 in the evening of 30 June 2020. According to the HYSPLIT backward trajectory analysis in Fig 2a the airmass was not in contact to any populated region during the last 10 days. Such clean conditions were frequently observed from the end of May to mid-July 2020.

435   On 5 August 2020, the atmosphere was significantly polluted above 1.5 km height (Fig. 1). HYSPLIT backward trajectories in Fig 2b indicate air mass transport from central and eastern Siberia at 2 km height. The same holds for 4 km height (not shown). The source identification method developed by Radenz et al. (2021) was applied in Fig. 3 to identify the aerosol sources for all heights in the troposphere. The length of each bar for the different heights indicates the time that the air mass spent at heights below 2 km during the long-distance travel and thus were able to accumulate aerosol pollution over the
440   Arctic Ocean, adjacent continental sites (savanna and shrubland at high latitudes), and regions further south (grass/cropland). As can be seen, the impact of continental airmasses increased with height and time. The air masses above 1.0 km (arriving at 18 and 21 UTC) were able to significantly uptake anthropogenic pollution, smoke and dust particles over Siberia. The MICROTOPS 500 nm AOT was close to 0.05 on 5 August. The integration of the lidar extinction profile yields a 532 nm

AOT of 0.047. By combining AOT (from MICROTOPS) and column backscatter (CB from lidar) we obtain a column lidar
ratio (AOT/CB) of 56.6 sr, a typical value for continental fine-mode-dominated aerosol (Mattis et al., 2004). The Ångström
exponent (MICROTOPS AOT, 440-870 nm) was around 1.7-1.9 in the evening of 5 August and thus in good agreement with
the backscatter-related Ångström exponent (355-1064 nm) of 1.4-2 in the height range from 2-6 km as shown in Fig. 1b. The
particle depolarization ratio was low (0.02-0.03) which is indicative for an almost dust-free air mass.

On 10 September 2020, a pronounced haze layer between 1.2 to 3.5 km was observed (Fig. 1). HYSPLIT backward trajec-
tories for this case are shown in Fig. 2c and indicate a pollution transport mainly from northern and western Europe and North
America. Polarstern was close to 89°N on this day. The AOT of the pronounced haze layer was 0.03, the overall AOT close
to 0.035. By combing MICROTOPS AOT and lidar-derived column backscatter we obtained a column lidar ratio of 57.8 sr,
again a characteristic value for anthropogenic pollution. The moderately low Ångström exponent of 1.3 (MICROTOPS) and
around 1.4 (lidar) together with the enhanced particle depolarization ratio of 0.05-0.07 indicate a noticable contribution of
coarse-mode dust of about 5% to the backscatter and extinction coefficients.

It is notworthy to mention that the Arctic haze layers in winter showed the highest aerosol burden in the lowest 500-1000 m
of the troposphere with highest extinction coefficient of the order of 30-70 Mm^{-1} close to the surface, as will be discussed in
the next section. The contribution of the lowest 1 km to the total tropospheric 532 nm AOT was typically 0.03-0.05 in winter.
In summer, these near-surface aerosol layers are absent, probably as a result of very efficient wet removal by low-level clouds,
drizzle, fog, and liquid-water precipitation (Browse et al., 2012). The AOT for the lowest 1000 m of the atmosphere is of the
order of 0.002-0.004 in Fig. 1a and thus an order of magnitude lower than a typical marine AOT over the open ocean.

Figure 4, finally, shows a wildfire smoke layer in the upper troposphere measured on 19 September 2020. High extinction
coefficients up to 300 Mm^{-1} were observed at heights around 9 km. The resulting 532 nm AOT was 0.4. The HYSPLIT
backward trajectories in Fig. 5 point to North America as smoke source region. According to Hu et al. (2022), intensive
wildfires in California and Oregon injected large amounts of wildfire smoke into the atmosphere on 10 and 11 September
2020. Thick smoke layers at 5-10 km height were detected with CALIOP over the Pacific Ocean just west of the west coast of
North America (Hu et al., 2022). CALIOP particle linear depolarization ratios (PLDRs) decreased from initial values of 12-
14% at 532 nm on 10 September to <10% over the eastern USA on 14 September 2020. The volume depolarization ratios of
5% in Fig. 4a and respective particle depolarization ratios of 6-7% (not shown) are in good agreement with the decreasing trend
found in the CALIOP PLDR observations over the United States. Hu et al. (2022) mentioned that pyrocumulonimbus (pyroCb)
development occurred on 9 September and that the smoke was trapped over the eastern Pacific Ocean on 7-11 September due
to cyclone activity. It remains open to what extent strong convective motions were responsible for smoke lofting up to the upper
troposphere. Enhanced PLDR values (>5%) indicate non-spherical smoke particles which are usually observed in the upper
troposphere when fast smoke lofting into the dry upper troposphere occurs. The decreasing PLDR values (with increasing
travel time) reflect the aging of smoke particles. They become increasingly compact and spherical with time.

Similar smoke conditions as observed over the central Arctic in September 2020 were also reported by Chazette et al. (2018).
These authors detected wildfire smoke layers over northern Norway in May 2016. The smoke originated from North America

and was found between 6 and 8.5 km height. The smoke showed slightly enhanced PLDR values and particle extinction coefficients up to $100 \, \text{Mm}^{-1}$.

4.2 MOSAiC annual cycle: Profiles of backscatter and extinction coefficients

The annual cycle of aerosol optical properties during the MOSAiC year is shown in Figs. 6 and 7. Monthly and 2-month mean backscatter and extinction profiles are presented. We considered all lidar observational periods with cloudfree conditions, lasting at least for 60 minutes. In situations with extended cloudfree weather conditions (over several days), more than one backscatter profile per day was considered (separated by at least six hours). In numbers, 12 lidar observations in October, 15 in November, 48 in December 2019, 8 in January, 15 in February, 10 in March, and 9 observations in April 2020 were possible. During the cloudy and foggy summer half year, 7 observations in May, 10 in June, 7 in July, 2 in August, and 5 observations in September 2020 could be included in the computation of the monthly mean and two-month mean backscatter profiles.

Figure 6 provides an overview of the year-around backscatter conditions up to 20 km height. One of the MOSAiC highlights was the detection of a pronounced and persistent Siberian wildfire smoke layer in the upper troposphere and lower stratosphere (UTLS) over the North Pole region from October 2019 to May 2020. Volcanic sulfate aerosol caused by the eruption of the Raikoke volcano in June 2019 contributed as well, mainly at heights >11 km height. This unique event was discussed in detail by Ohneiser et al. (2021), and in a recent comment letter by Ansmann et al. (2023). However, the highest tropospheric aerosol backscatter values were observed in the lowest 2.5 km during the winter half year in Fig. 6. Long range transport of aerosol pollution from the surrounding continents was responsible for these high backscatter levels.

Figure 7 focuses on tropospheric aerosols. The same MOSAiC profiles as in Fig. 6 are shown, however, now up to 10 km height in terms of the particle extinction coefficient. The backscatter coefficients in Fig. 6 were multiplied by an extinction-to-backscatter ratio (lidar ratio) of 55 sr. The lidar ratio may vary between 40-70 sr, thus the uncertainty in the extinction values is of the order of 25%.

The most striking feature in Fig. 7 is the strong decrease of the particle extinction coefficient with height during the winter months (Arctic haze season) when aged anthropogenic aerosol, soil dust, and biomass burning smoke is transported into the Arctic from the surrounding continents (North America, Asia, Europe) (Stohl, 2006; Willis et al., 2018; Engelmann et al., 2021). Most of the pollution reaching Polarstern at lower heights in the MOSAiC winter 2019-2020 originated from northern Asia (Creamean et al., 2022; Boyer et al., 2023). Arctic haze events observed on 4 February and 4 March 2020 were discussed in Engelmann et al. (2021). The largest extinction coefficients occurred close to the surface where the extinction values were as high as $100 \, \text{Mm}^{-1}$ (a typical value for Leipzig, Germany, in central Europe) in extreme situations. The extinction minimum was given at 4-5 km with values close to $1 \, \text{Mm}^{-1}$. Higher up, the UTLS wildfire smoke caused a re-increase in the particle extinction values. Stable atmospheric conditions with a low amount of precipitation and correspondingly weak removal of particles by ice-phase cloud scavenging and cloud-related deposition processes favors long range transport of aerosol pollution from the industrial centers in the northern hemisphere towards the central Arctic during winter (Browse et al., 2012). Removal of aerosol pollution by dry deposition (caused by downward mixing of particles and removal at the surface) is also low in winter over the snow and ice-covered regions (Willis et al., 2019). The less well-defined extinction profile structures observed

from March to May 2020 in Fig. 7 occurred during the phase when the rather strong polar vortex weakened in March and collapsed around 20 April 2020. The extremely strong polar vortex developed end of December 2019 and vanished completely in the beginning of May 2020 (Ohneiser et al., 2021; Rinke et al., 2021). Downward mixing of the UTLS pollution towards lower troposphere heights obviously occurred in March-May 2020.

During the summer months (June-August), aerosol layering is very different and the aerosol particle number concentration especially in the lowest 1 km was roughly an order of magnitude lower than during the winter period. This finding is in full agreement with the modeling study of Browse et al. (2012). They summarized that the seasonal cycle in Arctic aerosol is typified by high number concentrations of aged anthropogenic particles transported from lower latitudes in the late Arctic winter and early spring followed by a sharp transition to low concentrations of locally sourced particles in the summer. Wet scavenging processes have a strong impact on the seasonal variation in the aerosol conditions. Browse et al. (2012) show that the transition from high wintertime number concentrations to low concentrations in the summer is controlled by the transition from ice-phase cloud scavenging to the much more efficient warm cloud scavenging in the late spring troposphere. This seasonal cycle is amplified further by the appearance of warm drizzling cloud in the summer boundary layer. Low level liquid clouds and fog are ubiquitous in Arctic regions in summer and autumn.

The increased extinction coefficients above 4 km height in June-July and August-September are partly caused by wildfires, especially in August and September 2020. Record-breaking smoke conditions as in the summer of 2019, however, did not occur in 2020.

In Fig. 8, we compare the MOSAiC winter (December to February) and summer (June to August) height profiles of the particle extinction coefficient with respective long-term (2006-2019) winter and summer profiles derived from polar observations with the spaceborne lidar CALIOP (Yang et al., 2021). In this way, we can check to what extent unusual or typical aerosol condition were observed during the MOSAiC year. In the CALIOP-MOSAiC comparison, one has to keep in mind that the CALIOP profiles in Fig. 8 are mean profiles for the Arctic region from 65°-82°N (Yang et al., 2021). The impact of long range transport of aerosol pollution from mid to high northern latitudes is probably larger on the CALIOP observations than on the MOSAiC lidar observations from 80°-90°N. Furthermore, the tropospheric observations with a downward pointing spaceborne lidar CALIOP are less affected by low clouds and fog conditions than the MOSAiC observations with a ground-based lidar.

As can be seen, the MOSAiC observations in the lowermost 3 km during the winter months 2019-2020 agree very well with the 13-year mean profile observations from space. Arctic haze conditions seem to vary not much from year to year. The comparably low MOSAiC extinction in the 3-8 km height range in the winter of 2019-2020 may be partly related to the occurrence of the rather strong polar vortex in 2020, which may have prohibited the transport of aerosol pollution from the south towards the North Pole at heights >3 km. The re-increase of the aerosol extinction coefficient with height (above 7-8 km) in the MOSAiC winter 2019-2020 is caused by the presence of the persistent 2019-2020 UTLS wildfire smoke layer (Ohneiser et al., 2021). In the summer of 2020, the lower troposphere up to 6 km height between 80° and 90° N was obviously much cleaner than described by the 14-year (2006-2019) summer mean CALIOP extinction values for the latitudinal belt from 65°-82°N.

4.3 MOSAiC annual cycle: Aerosol optical thickness

A number of reports on Arctic aerosol optical properties are available from sunphotometer observations (e.g., Tomasi et al., 2012, 2015). Recently, Xian et al. (2022a, b) combined Aerosol Robotic Network (AERONET) observations (Holben et al., 1998) with aerosol modeling to study trends and changes in the Arctic aerosol conditions during the last 20 years. However, all these photometer observations were restricted to sun light conditions. No observation are possible from October to February in the central Arctic. Lidar observations from ground and space can fill this gap.

Figure 9 shows the AOT annual cycle for the MOSAiC year 2019-2020 derived from the Polarstern lidar observations. Several AOT time series for different vertical columns are presented. The AOTs were calculated from the monthly mean height profiles of the extinction coefficient. In contrast to Fig. 7, we used a lidar ratio of 55 sr in the conversion of backscatter to extinction coefficients for heights <5 km only. For the heights above >5 km, we used a smoke lidar ratio of 85 sr (Ohneiser et al., 2021). We further assumed that the backscatter coefficient at the minimum measurement height of about 100 m represents the backscatter conditions at the surface as well.

As was shown in Fig. 7, the main Arctic aerosol layer extended from the surface to the middle of the free troposphere. The annual AOT cycle of this layer (up to 5 km height) is very pronounced in Fig. 9. Arctic haze caused a 532 nm AOT of 0.05-0.06 during the MOSAiC winter and spring months. In summer (June-July, August-September), the AOT (for the height range up to 5 km) decreases to values close to 0.02 because of the effective removal of aerosol pollution from the atmosphere. The enhanced AOTs in April und May 2020 for the height range for 0-5 km were obviously dominated by downward mixing of the UTLS smoke towards lower heights.

The tropospheric AOT for the height range up to 10 km was strongly influenced by the UTLS wildfire smoke from October 2019 until May 2020. The AOT for the 0-20 km height range stops in April 2020 in Fig. 9 because a clear difference between the overall 0-20 km AOT and the 0-10 km AOT was no longer visible in the lidar data. The UTLS smoke layer dissolved after the collapse of the polar vortex end of April 2020.

The annual cycle of the AOT for the height range from the surface to 5 km is in good agreement with the 2006-2019 mean AOT obtained from the CALIOP observations. It needs to be mentioned here that CALIOP well detects the backscatter from the lower troposphere up to 5 km height, but is not very sensitive to weak backscatter contributions from the upper troposphere and lower stratosphere. Undetected aerosol contributions to the total AOT are typically of the order of 0.03 at 532 nm according to studies of Kim et al. (2017) and Toth et al. (2018). This bias explains to a large extent the difference between the MOSAiC AOTs (for the 0-10 km height range) and the CALIOP AOTs.

The MOSAiC AOT summer values (0-10 km, June-September 2020, 80°-90°N) of about 0.04 are lower than respective long-term Arctic AERONET sunphotometer observations. The long-term mean 500 nm AOTs are 0.06 to 0.07 at Thule (76.5°N, 68.7°W) and Ittoqqortoormiit (latitude 70.5°N, 22°W) for the summer half year (Xian et al., 2022a). According to the MICRO-TOPS II observations aboard Polarstern, the mean 500 nm AOT for June-July 2020 (based on 475 observations on 5 different days in June and 5 days in July, between 80° and 82°N) was 0.055±0.014. For the August-September 2020 period (185 ob-

servations on 3 different days in August and 4 days in September, mostly betweeen 85°-90°N) we obtained a 500 nm AOT of 0.051±0.015.

5   Observations, part 2: MOSAiC time series of cloud-relevant aerosol properties

In part 2 of the result sections, we present our lidar retrieval products regarding CCN and INP number concentrations. We include the MOSAiC in situ observations of the particle number concentrations $n_{50,\mathrm{dry}}$ (Boyer et al., 2023) and of ice nucleating particles n_{INP} (Creamean et al., 2022) aboard Polarstern into this discussion. We should emphasize that the lidar observations, performed during 1-3-hour-long cloudfree situations, were inhomogeneously distributed over the MOSAiC months and seasons while the in situ observations were regularly conduced day by day disregarding the weather conditions.

5.1   CCN number concentration at the surface, 250 m, and 2000 m height

In Fig. 10, lidar-derived time series of $n_{50,\mathrm{dry}}$, i.e., of n_{CCN} for a supersaturation of 0.2% at 250 m and 2000 m height (Sect. 3.3) and monthly means of $n_{50,\mathrm{dry}}$ measured in situ aboard Polarstern (Sect. 2.5) are shown. As mentioned, we selected the 250 and 2000 m height levels to show aerosol conditions relevant for the formation of low-level clouds and stratiform mixed-phase clouds in the lower free troposphere, respectively. To minimize the impact of even weak fog events, we considered lidar observations with a 532 nm backscatter coefficient of $<1\,\mathrm{Mm}^{-1}\,\mathrm{sr}^{-1}$ or extinction coefficients $<55\,\mathrm{Mm}^{-1}$, only. Thus, after conversion of the extinction coefficients, only $n_{50,\mathrm{dry}}$ values $<700\,\mathrm{cm}^{-3}$ remained.

In accordance with the observations of optical properties in Fig. 8, strong differences in the CCN number concentration between winter and summer are found at 250 m height. The $n_{50,\mathrm{dry}}$ or n_{CCN} values were mostly in the range of 50-500 cm^{-3} in the period from November 2019 to April 2020 and between 10-100 cm^{-3} during the summer months when marine CCNs dominate in the ABL. Such a strong contrast between winter and summer is not found at the 2000 m height level. Here, the $n_{50,\mathrm{dry}}$ values were mostly between 30-100 cm^{-3}. The winter (December to February) mean $n_{50,\mathrm{dry}}$ values (and corresponding SDs values) are 113±71 cm^{-3} (in situ, surface), 222±121 cm^{-3} (lidar, 250 m height), and 62±41 cm^{-3} (lidar, 2000 m height). The respect summer (June-August) values are 86±102 cm^{-3} (in situ, surface), 58±35 cm^{-3} (lidar, 250 m height), and 46±31 cm^{-3} (lidar, 2000 m height). The atmospheric variability, reflected in the SD values, is of the order of 50-100% around the mean values.

Direct in situ CCN observations aboard Polarstern (Dada et al., 2022) indicate that the background aerosol CCN values (for a supersaturation level of 0.2-0.3%) increased from $<50\,\mathrm{cm}^{-3}$ in October-December 2019, to about 100 cm^{-3} in Januray-March 2020, and 100-200 cm^{-3} in April and the first half of May 2020. Many short-term CCN number concentration peaks around 200-300 cm^{-3} (November-December), 400-550 cm^{-3} (January-February) and even 650 cm^{-3} (April 2020) were measured aboard Polarstern. Similar features (increasing values with time) are visible in the lidar observations at 250 m height in Fig. 10.

The lidar-derived winter values for $n_{50,\mathrm{dry}}$ at 250 m height are about a factor of 2 higher than the respective in-situ-measured winter $n_{50,\mathrm{dry}}$ values. The most likely reason for this bias is that the extinction-to-n_{50} conversion factor (in the lidar data analysis) was derived from summertime AERONET observations and the respective conversion factor for the dominating

aerosol type in winter (Arctic haze) was obviously about a factor of 2 lower than the summer aerosol conversion factor. As mentioned in Sect 3.3, the extinction-to-number-concentration conversion factor is very sensitive to the dominating particle size distributions (and changes from winter to summer size distributions). The summer deviations between the surface observations and lidar measurements at 250 m heigt are mainly caused by the low number of lidar observations (very low number of cloudfree periods during the summer months) compared to the high number of daily in situ measurements.

The MOSAiC observations were found to be in good agreement with other measurements in remote areas at high latitudes far away from centers of anthropogenic haze. Tatzelt et al. (2022) presented shipborne in situ measurements of CCN number concentrations conducted in the Southern Ocean during the Antarctic Circumnavigation Expedition (ACE) from December 2016 to March 2017 (summer season). They found mostly CCN values of 50-200 cm^{-3} for 0.2% supersaturation, but sometimes also more than 500 cm^{-3} or less than 5 cm^{-3}. Herenz et al. (2018) and Chang et al. (2022) performed observations of CCN number concentrations in the Canadian Arctic in May 2014 and July-August 2016, respectively, and found CCN number concentrations mostly from 20-150 cm^{-3} (Herenz et al., 2018) and 20-80 cm^{-3} (Chang et al., 2022). Hartmann et al. (2021) reported CCN concentrations from almost zero to 250 cm^{-3} ($S_{\mathrm{WAT}} = 1.002$) in the European Arctic at latitudes up to 83.7°N in May–July 2017.

5.2 INP number concentration at the surface, 250 m, and 2000 m height

Guided by our discussion in Sect. 1 about the different INP types in the Arctic ABL, the lower free troposphere, and in the upper Arctic troposphere, we performed the INP-related lidar data analysis separately for a near-surface height level (250 m), a height level in the lower free troposphere (2000 m) and for a height level close to the Arctic tropopause.

In Sect. 3.4.1, the immersion freezing INP parameterization applied to convert the lidar backscatter coefficients in the lower troposphere into INP number concentrations was described. The same lidar data as used in Sect. 5.1 were considered here. The lidar profiles (averaged over 1-3 hours) were now converted into particle surface area concentrations s_{dry} (by using the Arctic aerosol conversion factor c_{s} in Table 2). As mentioned in Sect. 3.4.1, the conversion factor c_{s} (input in INP retrieval) is almost insensitive to details in the Arctic particle size distribution so that s_{dry} can be obtained with a comparably low uncertainty of $\leq 25\%$, disregarding changes in the Arctic aerosol microphysical properties from winter to summer.

Figure 11 provides a representative view on the annual cycle of INP conditions in the central Arctic in the lowermost 3 km, i.e., in the height range in which mixed-phase clouds usually form. We considered typical ice nucleation temperatures, i.e., winter cloud top temperatures of $-25°C$ and summer cloud top temperatures of $-10°C$ at 250 m and $-15°C$ at 2000 m. We assume that immersion freezing starts at the coldest point of the cloud, i.e., at cloud top.

Eq. (5) in Sect. 3.4.1 was used to computed dust-related INP number concentrations at 250 m (autumn, winter, and spring months) and at 2000 m (all seasons). We assume that only clay mineral dust particles can serve as INPs in autumn, spring and winter months and ignore the contribution of agricultural soil dust. We adjusted the estimated INP time series for the 250 m height level in Fig. 11 to the in-situ-measured INP concentrations (for the time period from October 2019 - April 2020) by varying the dust fraction a_{frac} in Eq. (5). In this way we found a dust fraction of 1%. This is in agreement with the lidar

observations indicating low dust fractions, clearly below 5%. The dust aging impact was considered by assuming $f_{\text{age}} = 0.2$

645 (Augustin-Bauditz et al., 2014; Wex et al., 2014).

The INP parameterization for sea spray aerosol was applied to estimate the INP number concentration in the ABL during the summer months (June-August 2020). No adjustment to the in-situ measured INP concentration was performed here. In summer, we assume that continental aerosol particles (and thus dust particles) are absent in the Arctic ABL so that the aerosol in the lowermost tropospheric layer is of local marine origin ($a_{\text{frac}} = 1.0$ in Eq. 5).

650 As can be seen in Fig. 11, weakly varying INP number concentrations were observed at all three height levels (surface, 250 m, 2000 m height) from November 2019 to April 2020. This may be related to the stable weather patterns that were widely controlled by the strong, long-lasting winter polar vortex. The difference between the 250 m and 2000 m INP number concentrations (October-May) is related to the strong decrease of the particle number concentration with height as discussed in Sect. 4.2 and shown in Figs. 6 and 7.

655 The winter (December to February) mean INP number concentrations and corresponding SD values are 0.039 ± 0.02 cm^{-3} (in situ, surface, $-25°$C), 0.054 ± 0.042 cm^{-3} (lidar, 250 m height, $-25°$C, 1% dust), and 0.011 ± 0.0073 cm^{-3} (lidar, 2000 m height, $-25°$C, 1% dust). In contrast, the summer (June-August) values are 0.00031 ± 0.00081 cm^{-3} (in situ, surface, $-10°$C), 0.000019 ± 0.000012 cm^{-3} (lidar, 250 m height, $-10°$C, SSA), and 4.0E-7$\pm$2.8E-7 cm^{-3} (lidar, 2000 m height, $-15°$C, 1% dust). The natural (atmospheric) variability, indicated by SD, is of the order of 50-100% around the mean INP values.

660 The drop in the INP number concentration by 2-3 orders of magnitude in the ABL (surface, 250 m observations) from winter to summer is to a large part related to the change in the assumed increase of the cloud top temperatures from $-25°$C to -10 to $-15°$C. The INP number concentration roughly decreases by an order of magnitude when the cloud top temperature increases by 5 K. The effective wet removal of continental aerosol during long range transport to the central Arctic in summer (Browse et al., 2012) also contributes to this strong difference between the winter and summer ABL INP levels.

665 In Fig. 12, we show ABL INP time series for fixed temperatures of $-15°$C and $-25°$C to better see the impact of the different INP aerosol types (dust vs SSA) on ice nucleation in the boundary layer. At the low temperature of $-25°$C, the ice activity of SSA (summer) and clay mineral dust particles (winter, 1% fraction) are not very different, especially not in the case of the in situ observations. A pronounced annual cycle is visible in the INP time series for $-15°$C in Fig. 12. The estimated SSA INP values and the measured INP number concentrations show a maximum during the summer season. The rather low dust INP number

670 concentrations for $-15°$C results from the assumption in the INP parameterization (Eq. 5) that dust particles are exclusively kaolinite particles which are less efficient immersion freezing INPs at temperatures above $-20°$C. The in situ observations aboard Polartsern point to the presence of agricultural soil dust particles as well. The uncertainty in lidar-derived INP estimates is generally large because of the unknown mixture of dust components far away from the main dust source regions and the missing information regarding the impact of aging and cloud processing effects on the ice nucleation efficiency.

675 The hypothesis that biogenic INPs dominated the INP number concentrations in summer was already discussed by Creamean et al. (2022). The authors showed time series of n_{INP} for temperatures of $-10, -12.5, -15, -20, -22.5,$ and $-25°$C from October 2019 to September 2020. Only during the summer months (June to August), INPs were observed for high temperatures

of -10 and -12.5°C. In winter, the INP number concentrations were close to zero for these high temperatures because of the absence of biogenic aerosol components and because dust particles are not very ice-active at temperatures > -15°C.

680   The obviously different ice nucleation conditions in the ABL and in the layer above the ABL (with dust as the main INP type) in summer were also noticed by Griesche et al. (2021) who observed strong differences in the ice nucleation characteristics of summer mixed-phase clouds developing in an air mass coupled to the surface aerosol conditions and clouds which were decoupled from local aerosol conditions. The decoupled cloud systems showed similar properties as continental mixed-phase clouds, e.g., over Leipzig in Germany.

685   The MOSAiC observations as presented in Figs. 11 and 12 for -25°C are in good agreement with other INP measurements at high latitudes, far away from strong sources of pollution. Tatzelt et al. (2022) presented shipborne observation of INP number concentrations conducted in the Southern Ocean during ACE and found a strong accumulation of values between 0.05 and 0.1 L^{-1} (interquartile range) for the temperature of -25°C. Observations at Ny-Ålesund (78.9°N, 11.9°E) in Svalbard, Norway, in October-November 2019 and March-April 2020 yielded INP number concentrations mostly in the range from 0.13-0.3 L^{-1}

690   (interquartile range) between 6 October and 15 November 2019 and from 0.2-0.55 L^{-1} between 16 March and 22 April 2020 for the temperature of -25°C (Li et al., 2022). The Polarstern was more than 500 km north of Ny-Ålesund until April 2020. Si et al. (2019) reported INP number concentrations accumulating from 0.04-0.4 L^{-1} for -25°C, measured in the Canadian central Arctic (82.5°N, 62.5°W) during March 2016. Hartmann et al. (2021) found INP values of 0.03-2 L^{-1} for -25°C during a Polarstern cruise in the European Arctic up to 83.7°N in May-July 2017. Finally, Sze et al. (2023) analyzed two-year-

695   long INP measurements (from July 2018 to September 2020) at Villum 5 Research Station in Northern Greenland (81.6°N, 16.7°W). These observations suggest INP number concentrations mainly from 0.03-0.7 L^{-1} at -25°C. A clear indication for the dominance of biogenic INPs during the summer months was highlighted.

5.3   INP number concentration close to the tropopause

Cirrus formation processes in polar regions are poorly characterized by observations. The nucleation of first ice crystals, the

700   subsequent formation of extended cirrus layers, and the evolution of ice virga have a rather sensitive impact on the water cycle in the entire tropospheric column, influence the formation of cloud layers in the middle and lower troposphere by seeder-feeder effects and thus the radiation and precipitation fields over Arctic regions in a very complex way. The limited knowledge of all these processes hinders a proper simulation of polar clouds in the climate system. The lack of knowledge is particularly acute for the winter halfyear. The situation improved since spaceborne CALIOP (aerosol and cloud lidar) and CloudSat (cloud radar)

705   (Stephens et al., 2002) observations became available in 2006. Grenier et al. (2009) and Jouan et al. (2012, 2014) performed first systematic polar studies regarding the influence of aerosol particles on ice nucleation and cirrus microphysical properties based on CALIOP and CloudSAT observations.

Besides aged dust and soot particles, which are the most likely INP types at cirrus level at temperatures around and below -50°C, wildfire smoke should also be considered when dealing with aerosol-cirrus interaction, and should thus be implemented

710   in climate models in future. Aged wildfire smoke in the upper troposphere and stratosphere consists mainly of organic material.

Jahn et al. (2020) and Jahl et al. (2021) hypothesized that aged smoke particles contain minerals and that these components determine the smoke INP efficacy. How relevant this aspect is remains to be shown.

Figure 13 shows the MOSAiC time series of smoke INP estimates close to the tropopause from October 2019 to the beginning of May 2020, and then again in September 2020. In addition, mineral dust INP estimates for the summer months from June to August 2020 are included in the figure.

Each lidar data point in Fig. 13 represents a several hour observation (Ohneiser et al., 2021). The dust and smoke INP retrieval scheme (DIN parameterization) was explain in Sect. 3.4.2. The lidar-derived INP estimation is based on the simulation of gravity-wave-induced air parcel lofting over $\Delta t = 35$ s (mineral dust) and 88 s (smoke) for a given mean updraft speed of 30 cm/s (mean value for the first quarter of the gravity wave period of 1200 s). Within 35 s and 88 s the air parcel ascends by 16 m and 35 m, respectively, RH increases from $RH_{ICE,on}$ to the maximum RH_{ICE}, before the simulation is terminated. The values for T and the RH range from the $RH_{ICE,on}$ to the maximum RH_{ICE} in our ice nucleation simulation are given in Fig. 13. We assume a dust fraction a_{frac} of 5% to the total particle surface area during the summer months and also considered dust particle aging ($f_{age} = 0.2$) in Eq. (6). In the case of smoke, $a_{frac} = 1.0$ and $f_{age} = 1.0$. We arbitrarily terminated the INP computation when the INP concentration reached 30 L^{-1} in the case of an assumed total particle surface area concentration $s_{dry} = 25$ μm^2 cm^{-3} for reasons given in Sect. 3.4.2. By using the fixed INP integration times of 35 s and 88 s in Fig. 13, the INP values are directly linked to the observed aerosol particle surface area concentration. In this way, the natural variability in the atmospheric aerosol conditions and respective ice nucleation conditions become visible.

We compared our gravity-wave-related INP estimation with INP number concentrations obtained with the DIN parameterization of Ullrich et al. (2017) for mineral dust. The Ullrich INP parameterization was applied in the cirrus closure studies presented by Ansmann et al. (2019b). For $T = 208K$ and RH_{ICE} of 107, 109, 111, and 112%, we obtain INP number concentrations of 1.3, 5.5, 19, and 32 L^{-1}, respectively, for the same dust surface area conditions ($s_{dry} = 25$ μm^2 cm^{-3}, 5% dust fraction, aging factor of 0.2) used in the gravity wave simulation, in which we yielded 30 INPs per liter. The agreement between the two independent estimations of the INP number concentrations is good when keeping in mind that the overall uncertainty in any INP estimation is at least one order of magnitude.

As can be seen in Fig. 13, INP number concentrations may have been as high as 1-30 L^{-1} over months in the upper troposphere. These INP number concentrations are high enough to influence cirrus evolution (Spichtinger and Cziczo, 2010). To our opinion, the presence of 1-30 INPs per liter are even sufficient to suppress homogeneous freezing. For homogeneous ice nucleation a supersaturation of $S_{ICE} > 1.5$ is required at $-65°C$ (Koop et al., 2000). The INP values of 1-30 L^{-1} are in consistency with MOSAiC lidar-radar-based retrievals of ice crystal number number concentrations, n_{ICE}, following (Bühl et al., 2019). An example of the retrieval of n_{ICE} in Arctic cirrus layers and ice virga zones is shown in Engelmann et al. (2021). Based in the analysis of 10 MOSAiC cirrus systems occurring in December 2019 and January-February 2020, we obtained typical n_{ICE} values of 0.1-10 L^{-1}. These low crystal number concentrations are a clear sign for heterogeneous ice nucleation. We applied the recently published CAPTIVATE (Cloud, Aerosol and Precipitation from mulTiple Instruments using a VAriational TEchnique) algorithm (Mason et al., 2023) to the combined MOSAiC lidar-radar cirrus data sets as well to estimate n_{ICE} profiles and found good overall agreement with the results obtained with the approach of Bühl et al. (2019).

The MOSAiC radiosonde observations (Maturilli et al., 2021) support that wildfire smoke was the dominating INP typ from October 2019 to May 2020. The RH profiles frequently pointed to S_{ICE} values around 1.2 in the cirrus layers, a clear sign that ice-active dust particles were probably absent in these rather aged smoke plumes and thus not available for efficient ice nucleation. In the presence of dust particles, the S_{ICE} values are expected to be quickly reduced to values close to 1.0 because of strong ice nucleation already at $S_{ICE} \leq 1.1$ and sub subsequent water vapor deposition on the freshly nucleated ice crystals (Murray et al., 2010; Engelmann et al., 2021). Thus, the observed high radiosonde S_{ICE} values are more consistent with the presence of pure smoke particles as INPs.

The final Fig. 14 shows an example of the impact of wildfire smoke on cirrus formation. Polarstern was at 88°N. Four to five days of continuous cirrus formation from 25-29 February 2020 are presented. The smoke layer is clearly visible in the lidar observations as yellow layer around 10 km height. Heterogeneous ice nucleation occurred in the yellow smoke layer at temperatures from −69 to −73°C and RH values (over water) between 65% and 72% in the height range from 9-10 km on 25-28 Februar 2020 according to the MOSAiC radiosonde observations. The respective ice supersaturation values were frequently between 1.15 and 1.35. Weak gravity-wave-induced lofting is then sufficient to trigger nucleation of ice crystals. Immediately after nucleation, the crystals grew fast by water vapor deposition on the crystals and started to fall out of the smoke layer. They formed long virga, partly visible down to heights of 6 km in Fig. 14. Below 6 km height, the air was dry and the crystals evaporated.

6   Summary

MOSAiC provided a unique opportunity to study vertical aerosol layering up to 30 km height in the central Arctic from 80°-90°N over a full year. Continuous observations (around the clock) of aerosol and cloud profiles with an advanced lidar-radar facility have been successfully performed aboard the German ice breaker Polarstern from October 2019 to September 2020. Such a comprehensive field campaign has never been conducted in the central Arctic before. Active remote sensing was required to obtain annual cycles of aerosol conditions with high vertical resolution. Sun photometers only cover the sun light seasons. Wide spread surface in situ aerosol observations only cover the aerosol conditions in the shallow ABL and thus do not allow us to draw general conclusions about Arctic aerosols and their impact on cloud processes in different tropospheric height regimes.

The lidar observations together with the in situ observations aboard Polarstern allowed a detailed characterization of the vertical distributions of optical, microphysical, and cloud-relevant aerosol properties. A strong decrease of aerosol pollution (anthropogenic haze, fire smoke, and a small fraction of soil dust) with height was found during the winter months (October 2019 to April 2020) up to about 4-5 km height. The aerosol number concentration decreased by an order of magnitude within 2 km. The minimum in 4-5 km heights separated the Arctic haze layers in the lower atmosphere from wildfire smoke in the upper troposphere and lower stratosphere. In summer, rather clean conditions prevailed in the ABL, obviously a result of efficient wet removal of aerosols from the lowest kilometer of the Arctic atmosphere. Lofted continental aerosol plumes occurred from time to time, mostly above 1 km height.

CCN and INP number concentrations were estimated from the lidar observations. The CCN number concentration was found to strongly drop with height in winter in line with the observed decrease of the aerosol backscatter and extinction coefficients. During summer, the CCN number concentration in the ABL was, on average, an order of magnitude lower than in winter. As an important fact regarding mixed-phase cloud formation in the ABL, our MOSAiC observations corroborate that the main ice-active aerosol type changes from dust particles (during the autumn, winter, and spring months) to sea spray aerosol containing biogenic substances during the summer season. At 2000 m height, continental aerosol seems to dominate CCN and INP number concentrations throughout the year. Our INP studies suggest that a few percent of aged dust particles (1-5% contribution to the total particle surface area concentration) are sufficient to control ice nucleation in the lower Arctic troposphere (≤ 3 km height) most of the time, except in summer (within the ABL).

As a highlight of MOSAiC, we observed a persistent wildfire smoke layer in the UTLS height range from the beginning of MOSAiC in October 2019 to May 2020 (Engelmann et al., 2021; Ohneiser et al., 2021; Ansmann et al., 2023). This aerosol had the potential to significantly influence cirrus formation at tropopause level. Besides soil dust and soot, wildfire smoke, originating from strong fires in North America and Siberia year by year now, should thus be considered in upper tropospheric ice formation in atmospheric models.

As an outlook, we are presently analyzing MOSAiC lidar and radar observations regarding aerosol-cloud interaction processes, separately for mixed-phase clouds in the lower troposphere and for upper tropospheric cirrus. First examples of this part of our MOSAiC data analysis were presented in Engelmann et al. (2021). The main findings regarding aerosol-cloud interaction will be published in several follow-up MOSAiC articles.

7 Data availability

Polly lidar observations (level 0 data, measured signals) are in the PollyNet database (Polly, 2022). All the analysis products are available at TROPOS upon request (polly@tropos.de) and at https://doi.pangaea.de/10.1594/PANGAEA.935539 (Ohneiser et al., 2021). MOSAiC radiosonde data are available at https://doi.org/10.1594/PANGAEA.928656 (Maturilli et al., 2021) Backward trajectory analysis has been performed by air mass transport computation with the NOAA (National Oceanic and Atmospheric Administration) HYSPLIT (HYbrid Single-Particle Lagrangian Integrated Trajectory) model (HYSPLIT, 2022). AERONET and MICROPTOPS observational data are downloaded from the respective data bases (AERONET, 2022; AERONET-MAN, 2022).

8 Author contributions

The paper was written and designed by AA, KO and RE. The aerosol data analysis was performed by KO, RE, MR, JMC, MCB, JB, CJ, and HGe. KO, RE, JMC, MCB, DAK, MR, PS, and UW were involved in the interpretation of the findings. RE, HGr, MR, JH, and DA took care of the lidar observations aboard Polarstern during MOSAiC. SD and MM were responsible

for high-quality MOSAiC Polarstern radiosonde launches. All coauthors were actively involved in the extended discussions
and the elaboration of the final design of the manuscript

9 Competing interests

Daniel A. Knopf is a member of the editorial board of Atmospheric Chemistry and Physics

10 Financial support

The Multidisciplinary drifting Observatory for the Study of the Arctic Climate (MOSAiC) program was funded by the German
Federal Ministry for Education and Research (BMBF) through financing the Alfred Wegener Institut Helmholtz Zentrum für
Polar und Meeresforschung (AWI) and the Polarstern expedition PS122 under grant N-2014-H-060_Dethloff. The lidar analy-
sis on smoke-cirrus interaction was further supported by BMBF funding of the SCiAMO project (MOSAIC-FKZ 03F0915A).
The radiosonde program was funded by AWI awards AFMOSAiC-1_00 and AWI_PS122_00, the U.S. Department of Energy
Atmospheric Radiation Measurement Program, and the German Weather Service. This project has also received funding from
the European Union's Horizon 2020 research and innovation program ACTRIS-2 Integrating Activities (H2020-INFRAIA-
2014 - 2015, grant agreement no. 654109). We gratefully acknowledge the funding by the Deutsche Forschungsgemeinschaft
(DFG, German Research Foundation) – project no. 268020496 - TRR 172, within the Transregional Collaborative Research
Center "ArctiC Amplification: Climate Relevant Atmospheric and SurfaCe Processes, and Feedback Mechanisms (AC)3". JMC
acknowledges support by U.S. Department of Energy's (DOE) Atmospheric Radiation Mission (ARM) (grant no. DE-AC05-
76RL01830 DE-SC0021034) and Atmospheric System Research (ASR) program (grant no. DE-SC0019745, DE-SC002204).
DAK acknowledges support by U.S. Department of Energy's (DOE) Atmospheric System Research (ASR) program, Office of
Biological and Environmental Research (OBER) (grant no. DE-SC0021034).

Acknowledgements. Data used in this article were produced as part of the international Multidisciplinary drifting Observatory for the Study
of the Arctic Climate (MOSAiC) with the tag MOSAiC20192020 and the Project_ID: AWI_PS122_00. We would like to thank everyone
who contributed to the measurements used here (Nixdorf et al., 2021). Radiosonde data were obtained through a partnership between the
leading Alfred Wegener Institute, the Atmospheric Radiation Measurement user facility, a U.S. Department of Energy facility managed by
the Biological and Environmental Research Program, and the German Weather Service (DWD). We would like to thank the RV Polarstern
crew for their perfect logistical support during the one-year MOSAiC expedition.

References

Abbatt, J. P. D., Leaitch, W. R., Aliabadi, A. A., Bertram, A. K., Blanchet, J.-P., Boivin-Rioux, A., Bozem, H., Burkart, J., Chang, R. Y. W., Charette, J., Chaubey, J. P., Christensen, R. J., Cirisan, A., Collins, D. B., Croft, B., Dionne, J., Evans, G. J., Fletcher, C. G., Galí, M., Ghahremaninezhad, R., Girard, E., Gong, W., Gosselin, M., Gourdal, M., Hanna, S. J., Hayashida, H., Herber, A. B., Hesaraki, S., Hoor, P., Huang, L., Hussherr, R., Irish, V. E., Keita, S. A., Kodros, J. K., Köllner, F., Kolonjari, F., Kunkel, D., Ladino, L. A., Law, K., Levasseur, M., Libois, Q., Liggio, J., Lizotte, M., Macdonald, K. M., Mahmood, R., Martin, R. V., Mason, R. H., Miller, L. A., Moravek, A., Mortenson, E., Mungall, E. L., Murphy, J. G., Namazi, M., Norman, A.-L., O'Neill, N. T., Pierce, J. R., Russell, L. M., Schneider, J., Schulz, H., Sharma, S., Si, M., Staebler, R. M., Steiner, N. S., Thomas, J. L., von Salzen, K., Wentzell, J. J. B., Willis, M. D., Wentworth, G. R., Xu, J.-W., and Yakobi-Hancock, J. D.: Overview paper: New insights into aerosol and climate in the Arctic, Atmospheric Chemistry and Physics, 19, 2527–2560, https://doi.org/10.5194/acp-19-2527-2019, 2019.

AERONET-MAN(2022): AERONET Maritime Aerosol Network database, available at: https://aeronet.gsfc.nasa.gov/new_web/maritime_aerosol_network.html, last access: 4 February, 2022.

AERONET(2022): Aerosol Robotic Network aerosol data base, available at: http://aeronet.gsfc.nasa.gov/, last access: 10 December, 2022.

Alpert, P. A. and Knopf, D. A.: Analysis of isothermal and cooling-rate-dependent immersion freezing by a unifying stochastic ice nucleation model, Atmospheric Chemistry and Physics, 16, 2083–2107, https://doi.org/10.5194/acp-16-2083-2016, 2016.

Alpert, P. A., Kilthau, W. P. and, O. R. E., Moffet, R. C., Gilles, M. K., Wang, B., Laskin, A., Aller, J. Y., and Knopf, D. A.: Ice-nucleating agents in sea spray aerosol identified and quantified with a holistic multimodal freezing model, Sci. Adv., 8, https://doi.org/10.1126/sciadv.abq6842, 2022.

Ansmann, A., Tesche, M., Althausen, D., Müller, D., Seifert, P., Freudenthaler, V., Heese, B., Wiegner, M., Pisani, G., Knippertz, P., and Dubovik, O.: Influence of Saharan dust on cloud glaciation in southern Morocco during the Saharan Mineral Dust Experiment, Journal of Geophysical Research: Atmospheres, 113, https://doi.org/10.1029/2007JD008785, 2008.

Ansmann, A., Tesche, M., Seifert, P., Althausen, D., Engelmann, R., Fruntke, J., Wandinger, U., Mattis, I., and Müller, D.: Evolution of the ice phase in tropical altocumulus: SAMUM lidar observations over Cape Verde, Journal of Geophysical Research: Atmospheres, 114, https://doi.org/10.1029/2008JD011659, 2009.

Ansmann, A., Mamouri, R.-E., Hofer, J., Baars, H., Althausen, D., and Abdullaev, S. F.: Dust mass, cloud condensation nuclei, and ice-nucleating particle profiling with polarization lidar: updated POLIPHON conversion factors from global AERONET analysis, Atmospheric Measurement Techniques, 12, 4849–4865, https://doi.org/10.5194/amt-12-4849-2019, 2019a.

Ansmann, A., Mamouri, R.-E., Bühl, J., Seifert, P., Engelmann, R., Hofer, J., Nisantzi, A., Atkinson, J. D., Kanji, Z. A., Sierau, B., Vrekoussis, M., and Sciare, J.: Ice-nucleating particle versus ice crystal number concentration in altocumulus and cirrus layers embedded in Saharan dust: a closure study, Atmospheric Chemistry and Physics, 19, 15 087–15 115, https://doi.org/10.5194/acp-19-15087-2019, 2019b.

Ansmann, A., Ohneiser, K., Mamouri, R.-E., Knopf, D. A., Veselovskii, I., Baars, H., Engelmann, R., Foth, A., Jimenez, C., Seifert, P., and Barja, B.: Tropospheric and stratospheric wildfire smoke profiling with lidar: mass, surface area, CCN, and INP retrieval, Atmospheric Chemistry and Physics, 21, https://doi.org/10.5194/acp-21-9779-2021, 2021.

Ansmann, A., Veselovskii, I., Ohneiser, K., and Chudnovsky, A.: Comment on "Stratospheric Aerosol Composition Observed by the Atmospheric Chemistry Experiment Following the 2019 Raikoke Eruption" by Boone et al., Journal of Geophysical Research: Atmospheres, 128, https://doi.org/10.1029/2022JD037xxx, accepted in July, 2023.

Augustin-Bauditz, S., Wex, H., Kanter, S., Ebert, M., Niedermeier, D., Stolz, F., Prager, A., and Stratmann, F.: The immersion mode ice nucleation behavior of mineral dusts: A comparison of different pure and surface modified dusts, Geophysical Research Letters, 41, 7375–7382, https://doi.org/10.1002/2014GL061317, 2014.

Baars, H., Kanitz, T., Engelmann, R., Althausen, D., Heese, B., Komppula, M., Preißler, J., Tesche, M., Ansmann, A., Wandinger, U., Lim, J.-H., Ahn, J. Y., Stachlewska, I. S., Amiridis, V., Marinou, E., Seifert, P., Hofer, J., Skupin, A., Schneider, F., Bohlmann, S., Foth, A., Bley, S., Pfüller, A., Giannakaki, E., Lihavainen, H., Viisanen, Y., Hooda, R. K., Pereira, S. N., Bortoli, D., Wagner, F., Mattis, I., Janicka, L., Markowicz, K. M., Achtert, P., Artaxo, P., Pauliquevis, T., Souza, R. A. F., Sharma, V. P., van Zyl, P. G., Beukes, J. P., Sun, J., Rohwer, E. G., Deng, R., Mamouri, R.-E., and Zamorano, F.: An overview of the first decade of Polly[NET]: an emerging network of automated Raman-polarization lidars for continuous aerosol profiling, Atmospheric Chemistry and Physics, 16, 5111–5137, https://doi.org/10.5194/acp-16-5111-2016, 2016.

Barahona, D., Molod, A., and Kalesse, H.: Direct estimation of the global distribution of vertical velocity within cirrus clouds, Sci. Rep., 7, https://doi.org/10.1038/s41598-017-07038-6, 2019.

Beck, I., Angot, H., Baccarini, A., Dada, L., Quéléver, L., Jokinen, T., Laurila, T., Lampimäki, M., Bukowiecki, N., Boyer, M., Gong, X., Gysel-Beer, M., Petäjä, T., Wang, J., and Schmale, J.: Automated identification of local contamination in remote atmospheric composition time series, Atmospheric Measurement Techniques, 15, 4195–4224, https://doi.org/10.5194/amt-15-4195-2022, 2022.

Bohlmann, S., Baars, H., Radenz, M., Engelmann, R., and Macke, A.: Ship-borne aerosol profiling with lidar over the Atlantic Ocean: from pure marine conditions to complex dust–smoke mixtures, Atmospheric Chemistry and Physics, 18, 9661–9679, https://doi.org/10.5194/acp-18-9661-2018, 2018.

Boyer, M., Aliaga, D., Pernov, J. B., Angot, H., Quéléver, L. L. J., Dada, L., Heutte, B., Dall'Osto, M., Beddows, D. C. S., Brasseur, Z., Beck, I., Bucci, S., Duetsch, M., Stohl, A., Laurila, T., Asmi, E., Massling, A., Thomas, D. C., Nøjgaard, J. K., Chan, T., Sharma, S., Tunved, P., Krejci, R., Hansson, H. C., Bianchi, F., Lehtipalo, K., Wiedensohler, A., Weinhold, K., Kulmala, M., Petäjä, T., Sipilä, M., Schmale, J., and Jokinen, T.: A full year of aerosol size distribution data from the central Arctic under an extreme positive Arctic Oscillation: insights from the Multidisciplinary drifting Observatory for the Study of Arctic Climate (MOSAiC) expedition, Atmospheric Chemistry and Physics, 23, 389–415, https://doi.org/10.5194/acp-23-389-2023, 2023.

Brock, C. A., Froyd, K. D., Dollner, M., Williamson, C. J., Schill, G., Murphy, D. M., Wagner, N. J., Kupc, A., Jimenez, J. L., Campuzano-Jost, P., Nault, B. A., Schroder, J. C., Day, D. A., Price, D. J., Weinzierl, B., Schwarz, J. P., Katich, J. M., Wang, S., Zeng, L., Weber, R., Dibb, J., Scheuer, E., Diskin, G. S., DiGangi, J. P., Bui, T., Dean-Day, J. M., Thompson, C. R., Peischl, J., Ryerson, T. B., Bourgeois, I., Daube, B. C., Commane, R., and Wofsy, S. C.: Ambient aerosol properties in the remote atmosphere from global-scale in situ measurements, Atmospheric Chemistry and Physics, 21, 15 023–15 063, https://doi.org/10.5194/acp-21-15023-2021, 2021.

Browse, J., Carslaw, K. S., Arnold, S. R., Pringle, K., and Boucher, O.: The scavenging processes controlling the seasonal cycle in Arctic sulphate and black carbon aerosol, Atmospheric Chemistry and Physics, 12, 6775–6798, https://doi.org/10.5194/acp-12-6775-2012, 2012.

Bühl, J., Seifert, P., Radenz, M., Baars, H., and Ansmann, A.: Ice crystal number concentration from lidar, cloud radar and radar wind profiler measurements, Atmospheric Measurement Techniques, 12, 6601–6617, https://doi.org/10.5194/amt-12-6601-2019, 2019.

Carlsen, T. and David, R. O.: Spaceborne Evidence That Ice-Nucleating Particles Influence High-Latitude Cloud Phase, Geophysical Research Letters, 49, e2022GL098 041, https://doi.org/10.1029/2022GL098041, e2022GL098041 2022GL098041, 2022.

Chang, R. Y.-W., Abbatt, J. P. D., Boyer, M. C., Chaubey, J. P., and Collins, D. B.: Characterizing the hygroscopicity of growing particles in the Canadian Arctic summer, Atmospheric Chemistry and Physics, 22, 8059–8071, https://doi.org/10.5194/acp-22-8059-2022, 2022.

Chazette, P., Raut, J.-C., and Totems, J.: Springtime aerosol load as observed from ground-based and airborne lidars over northern Norway, Atmospheric Chemistry and Physics, 18, 13 075–13 095, https://doi.org/10.5194/acp-18-13075-2018, 2018.

910 Choudhury, G., Ansmann, A., and Tesche, M.: Evaluation of aerosol number concentrations from CALIPSO with ATom airborne in situ measurements, Atmospheric Chemistry and Physics, 22, 7143–7161, https://doi.org/10.5194/acp-22-7143-2022, 2022.

Creamean, J., Barry, K., Hill, T., Hume, C., DeMott, P. J., Shupe, M. D., Dahlke, S., Willmes, S., Schmale, J., Beck, I., Hoppe, C. J. . M., Fong, A., Chamberlain, E., Bowman, J., Scharien, R., and Persson, O.: Annual cycle observations of aerosols capable of ice formation in central Arctic clouds, Nat. Commun., 13, https://doi.org/10.1038/s41467-022-31182-x, 2022.

915 Creamean, J. M., Kirpes, R. M., Pratt, K. A., Spada, N. J., Maahn, M., de Boer, G., Schnell, R. C., and China, S.: Marine and terrestrial influences on ice nucleating particles during continuous springtime measurements in an Arctic oilfield location, Atmospheric Chemistry and Physics, 18, 18 023–18 042, https://doi.org/10.5194/acp-18-18023-2018, 2018.

Creamean, J. M., Cross, J. N., Pickart, R., McRaven, L., Lin, P., Pacini, A., Hanlon, R., Schmale, D. G., Ceniceros, J., Aydell, T., Colombi, N., Bolger, E., and DeMott, P. J.: Ice Nucleating Particles Carried From Below a Phytoplankton Bloom to the Arctic Atmosphere, Geophysical
920 Research Letters, 46, 8572–8581, https://doi.org/10.1029/2019GL083039, 2019.

Cziczo, D. J., Froyd, K. D., Gallavardin, S. J., Möhler, O., Benz, S., Saathoff, H., and Murphy, D. M.: Deactivation of ice nuclei due to atmospherically relevant surface coatings, Environmental Research Letters, 4, 1–8, https://doi.org/10.1088/1748-9326/4/4/044013, 2009.

Dada, L., Angot, H., Beck, I., Baccarini, A., Quéléver, L. L. J., Boyer, M., Laurila, T., Brasseur, Z., Jozef, G., de Boer, G., Shupe, M. D., Henning, S., Bucci, S., Dütsch, M., Stohl, A., Petäjä, T., Daellenbach, K. R., Jokinen, T., and Schmale, J.: A central Arctic extreme aerosol
925 event triggered by a warm air-mass intrusion, Natur Commun., 13, https://doi.org/10.1038/s41467-022-32872-2, 2022.

Dahlkötter, F., Gysel, M., Sauer, D., Minikin, A., Baumann, R., Seifert, P., Ansmann, A., Fromm, M., Voigt, C., and Weinzierl, B.: The Pagami Creek smoke plume after long-range transport to the upper troposphere over Europe - aerosol properties and black carbon mixing state, Atmospheric Chemistry and Physics, 14, 6111–6137, https://doi.org/10.5194/acp-14-6111-2014, 2014.

de Boer, G., Morrison, H., Shupe, M. D., and Hildner, R.: Evidence of liquid dependent ice nucleation in high-latitude stratiform clouds from
930 surface remote sensors, Geophysical Research Letters, 38, https://doi.org/https://doi.org/10.1029/2010GL046016, 2011.

DeMott, P. J., Prenni, A. J., McMeeking, G. R., Sullivan, R. C., Petters, M. D., Tobo, Y., Niemand, M., Möhler, O., Snider, J. R., Wang, Z., and Kreidenweis, S. M.: Integrating laboratory and field data to quantify the immersion freezing ice nucleation activity of mineral dust particles, Atmospheric Chemistry and Physics, 15, 393–409, https://doi.org/10.5194/acp-15-393-2015, 2015.

DeMott, P. J., Hill, T. C. J., McCluskey, C. S., Prather, K. A., Collins, D. B., Sullivan, R. C., Ruppel, M. J., Mason, R. H., Irish, V. E., Lee,
935 T., Hwang, C. Y., Rhee, T. S., Snider, J. R., McMeeking, G. R., Dhaniyala, S., Lewis, E. R., Wentzell, J. J. B., Abbatt, J., Lee, C., Sultana, C. M., Ault, A. P., Axson, J. L., Martinez, M. D., Venero, I., Santos-Figueroa, G., Stokes, M. D., Deane, G. B., Mayol-Bracero, O. L., Grassian, V. H., Bertram, T. H., Bertram, A. K., Moffett, B. F., and Franc, G. D.: Sea spray aerosol as a unique source of ice nucleating particles, Proceedings of the National Academy of Sciences, 113, 5797–5803, https://doi.org/10.1073/pnas.1514034112, 2016.

Düsing, S., Wehner, B., Seifert, P., Ansmann, A., Baars, H., Ditas, F., Henning, S., Ma, N., Poulain, L., Siebert, H., Wiedensohler, A., and
940 Macke, A.: Helicopter-borne observations of the continental background aerosol in combination with remote sensing and ground-based measurements, Atmospheric Chemistry and Physics, 18, 1263–1290, https://doi.org/10.5194/acp-18-1263-2018, 2018.

Elementa(2022): Elementa: Science of the Anthropocene, MOSAiC overview articles in the Special Feature Collection to The Multidisciplinary Drifting Observatory for the Study of Arctic Climate (MOSAiC), https://doi.org/10.1525/elementa.2021.00060,10.1525/elementa. 2021.000046,10.1525/elementa.2021.00062, last access: 03 June, 2022.

945 Engelmann, R., Kanitz, T., Baars, H., Heese, B., Althausen, D., Skupin, A., Wandinger, U., Komppula, M., Stachlewska, I. S., Amiridis, V., Marinou, E., Mattis, I., Linné, H., and Ansmann, A.: The automated multiwavelength Raman polarization and water-vapor lidar Polly^{XT}: the neXT generation, Atmospheric Measurement Techniques, 9, 1767–1784, https://doi.org/10.5194/amt-9-1767-2016, 2016.

Engelmann, R., Ansmann, A., Ohneiser, K., Griesche, H., Radenz, M., Hofer, J., Althausen, D., Dahlke, S., Maturilli, M., Veselovskii, I., Jimenez, C., Wiesen, R., Baars, H., Bühl, J., Gebauer, H., Haarig, M., Seifert, P., Wandinger, U., and Macke, A.: Wildfire smoke, Arctic

950 haze, and aerosol effects on mixed-phase and cirrus clouds over the North Pole region during MOSAiC: an introduction, Atmospheric Chemistry and Physics, 21, https://doi.org/10.5194/acp-21-13397-2021, 2021.

Georgoulias, A. K., Marinou, E., Tsekeri, A., Proestakis, E., Akritidis, D., Alexandri, G., Zanis, P., Balis, D., Marenco, F., Tesche, M., and Amiridis, V.: A first case study of CCN concentrations from spaceborne lidar observations, Remote Sensing, 12, https://doi.org/10.3390/rs12101557, 2020.

955 Grenier, P., Blanchet, J.-P., and Muñoz-Alpizar, R.: Study of polar thin ice clouds and aerosols seen by CloudSat and CALIPSO during midwinter 2007, Journal of Geophysical Research: Atmospheres, 114, https://doi.org/https://doi.org/10.1029/2008JD010927, 2009.

Griesche, H. J., Seifert, P., Ansmann, A., Baars, H., Barrientos Velasco, C., Bühl, J., Engelmann, R., Radenz, M., Zhenping, Y., and Macke, A.: Application of the shipborne remote sensing supersite OCEANET for profiling of Arctic aerosols and clouds during *Polarstern* cruise PS106, Atmospheric Measurement Techniques, 13, 5335–5358, https://doi.org/10.5194/amt-13-5335-2020, 2020.

960 Griesche, H. J., Ohneiser, K., Seifert, P., Radenz, M., Engelmann, R., and Ansmann, A.: Contrasting ice formation in Arctic clouds: surface-coupled vs. surface-decoupled clouds, Atmospheric Chemistry and Physics, 21, 10 357–10 374, https://doi.org/10.5194/acp-21-10357-2021, 2021.

Haag, W. and Kärcher, B.: The impact of aerosols and gravity waves on cirrus clouds at midlatitudes, Journal of Geophysical Research: Atmospheres, 109, https://doi.org/10.1029/2004JD004579, 2004.

965 Haarig, M., Walser, A., Ansmann, A., Dollner, M., Althausen, D., Sauer, D., Farrell, D., and Weinzierl, B.: Profiles of cloud condensation nuclei, dust mass concentration, and ice-nucleating-particle-relevant aerosol properties in the Saharan Air Layer over Barbados from polarization lidar and airborne in situ measurements, Atmospheric Chemistry and Physics, 19, 13 773–13 788, https://doi.org/10.5194/acp-19-13773-2019, 2019.

Hartmann, M., Gong, X., Kecorius, S., van Pinxteren, M., Vogl, T., Welti, A., Wex, H., Zeppenfeld, S., Herrmann, H., Wiedensohler, A., and

970 Stratmann, F.: Terrestrial or marine – indications towards the origin of ice-nucleating particles during melt season in the European Arctic up to 83.7° N, Atmospheric Chemistry and Physics, 21, 11 613–11 636, https://doi.org/10.5194/acp-21-11613-2021, 2021.

Herenz, P., Wex, H., Henning, S., Kristensen, T. B., Rubach, F., Roth, A., Borrmann, S., Bozem, H., Schulz, H., and Stratmann, F.: Measurements of aerosol and CCN properties in the Mackenzie River delta (Canadian Arctic) during spring–summer transition in May 2014, Atmospheric Chemistry and Physics, 18, 4477–4496, https://doi.org/10.5194/acp-18-4477-2018, 2018.

975 Hofer, J., Althausen, D., Abdullaev, S. F., Makhmudov, A. N., Nazarov, B. I., Schettler, G., Engelmann, R., Baars, H., Fomba, K. W., Müller, K., Heinold, B., Kandler, K., and Ansmann, A.: Long-term profiling of mineral dust and pollution aerosol with multiwavelength polarization Raman lidar at the Central Asian site of Dushanbe, Tajikistan: case studies, Atmospheric Chemistry and Physics, 17, 14 559–14 577, https://doi.org/10.5194/acp-17-14559-2017, 2017.

Holben, B. N., Eck, T. F., Slutsker, I., Tanré, D., Buis, J. P., Setzer, A., Vermote, E., Reagan, J. A., Kaufman, Y. J., Nakajima, T., Lavenu,

980 F., Jankowiak, I., and Smirnov, A.: AERONET - A federated instrument network and data archive for aerosol characterization, Remote Sensing of Environment, 66, 1–16, https://doi.org/10.1016/S0034-4257(98)00031-5, 1998.

Hu, Q., Goloub, P., Veselovskii, I., and Podvin, T.: The characterization of long-range transported North American biomass burning plumes: what can a multi-wavelength Mie–Raman-polarization-fluorescence lidar provide?, Atmospheric Chemistry and Physics, 22, 5399–5414, https://doi.org/10.5194/acp-22-5399-2022, 2022.

985 HYSPLIT(2022): HYbrid Single-Particle Lagrangian Integrated Trajectory model, backward trajectory calculation tool, available at: http://ready.arl.noaa.gov/HYSPLIT_traj.php, last access: 20 November, 2022.

Ichoku, C., Levy, R., Kaufman, Y. J., Remer, L. A., Li, R.-R., Martins, V. J., Holben, B. N., Abuhassan, N., Slutsker, I., Eck, T. F., and Pietras, C.: Analysis of the performance characteristics of the five-channel Microtops II Sun photometer for measuring aerosol optical thickness and precipitable water vapor, Journal of Geophysical Research: Atmospheres, 107, AAC 5–1–AAC 5–17,

990 https://doi.org/https://doi.org/10.1029/2001JD001302, 2002.

Jahl, L. G., Brubaker, T. A., Polen, M. J., Jahn, L. G., Cain, K. P., Bowers, B. B., Fahy, W. D., Graves, S., and Sullivan, R. C.: Atmospheric aging enhances the ice nucleation ability of biomass-burning aerosol, Sci. Adv., 7, https://doi.org/10.1126/sciadv.abd3440, 2021.

Jahn, L. G., Polen, M. J., Jahl, L. G., Brubaker, T. A., Somers, J., and Sullivan, R. C.: Biomass combustion produces ice-active minerals in biomass-burning aerosol and bottom ash, Proc. Natl. Acad. Sci. U.S.A., 117, 21 928–21 937, https://doi.org/10.1073/pnas.1922128117,

995 2020.

Jimenez, C., Ansmann, A., Engelmann, R., Donovan, D., Malinka, A., Seifert, P., Wiesen, R., Radenz, M., Yin, Z., Bühl, J., Schmidt, J., Barja, B., and Wandinger, U.: The dual-field-of-view polarization lidar technique: a new concept in monitoring aerosol effects in liquid-water clouds – case studies, Atmospheric Chemistry and Physics, 20, 15 265–15 284, https://doi.org/10.5194/acp-20-15265-2020, 2020.

Jouan, C., Girard, E., Pelon, J., Gultepe, I., Delanoë, J., and Blanchet, J.-P.: Characterization of Arctic ice cloud properties observed during

1000 ISDAC, Journal of Geophysical Research: Atmospheres, 117, https://doi.org/https://doi.org/10.1029/2012JD017889, 2012.

Jouan, C., Pelon, J., Girard, E., Ancellet, G., Blanchet, J. P., and Delanoë, J.: On the relationship between Arctic ice clouds and polluted air masses over the North Slope of Alaska in April 2008, Atmospheric Chemistry and Physics, 14, 1205–1224, https://doi.org/10.5194/acp-14-1205-2014, 2014.

Kalesse, H. and Kollias, P.: Climatology of high cloud dynamics using profiling ARM Doppler radar observations, Journal of Climate, 26,

1005 6340–6359, https://doi.org/10.1175/JCLI-D-12-00695.1, 2013.

Kanitz, T., Seifert, P., Ansmann, A., Engelmann, R., Althausen, D., Casiccia, C., and Rohwer, E. G.: Contrasting the impact of aerosols at northern and southern midlatitudes on heterogeneous ice formation, Geophys. Res. Lett., 38, https://doi.org/10.1029/2011GL048532, 2011.

Kanitz, T., Ansmann, A., Engelmann, R., and Althausen, D.: North-south cross sections of the vertical aerosol distribution over the Atlantic

1010 Ocean from multiwavelength Raman/polarization lidar during Polarstern cruises, Journal of Geophysical Research: Atmospheres, 118, 2643–2655, https://doi.org/10.1002/jgrd.50273, 2013.

Kanji, Z. A., Ladino, L. A., Wex, H., Boose, Y., Burkert-Kohn, M., Cziczo, D. J., and Krämer, M.: Overview of ice nucleating particles, Meteorological monographs, 58, 1 – 33, https://doi.org/10.1175/AMSMONOGRAPHS-D-16-0006.1, 2017.

Kanji, Z. A., Sullivan, R. C., Niemand, M., DeMott, P. J., Prenni, A. J., Chou, C., Saathoff, H., and Möhler, O.: Heterogeneous ice nucleation

1015 properties of natural desert dust particles coated with a surrogate of secondary organic aerosol, Atmospheric Chemistry and Physics, 19, 5091–5110, https://doi.org/10.5194/acp-19-5091-2019, 2019.

Kawai, K., Matsui, H., and Tobo, Y.: Dominant Role of Arctic Dust With High Ice Nucleating Ability in the Arctic Lower Troposphere, Geophysical Research Letters, 50, e2022GL102 470, https://doi.org/10.1029/2022GL102470, e2022GL102470 2022GL102470, 2023.

Kim, M.-H., Omar, A. H., Vaughan, M. A., Winker, D. M., Trepte, C. R., Hu, Y., Liu, Z., and Kim, S.-W.: Quantifying the low bias of CALIPSO's column aerosol optical depth due to undetected aerosol layers, Journal of Geophysical Research: Atmospheres, 122, 1098–1113, https://doi.org/10.1002/2016JD025797, 2017.

Knopf, D. A. and Alpert, P. A.: A water activity based model of heterogeneous ice nucleation kinetics for freezing of water and aqueous solution droplets, Farad. Discuss., 165, 513–534, https://doi.org/10.1039/c3fd00035d, 2013.

Knopf, D. A. and Alpert, P. A.: Atmospheric ice nucleation, Nat. Rev. Phys., 5, 203–217, https://doi.org/10.1038/s42254-023-00570-7, 2023.

Knopf, D. A., Alpert, P. A., and Wang, B.: The role of organic aerosol in atmospheric ice nucleation: a review, ACS Earth and Space Chemistry, 2, 168–202, https://doi.org/10.1021/acsearthspacechem.7b00120, 2018.

Knust, R.: Polar Research and Supply Vessel POLARSTERN operated by the Alfred-Wegener-Institute, Journal of large-scale research facilities JLSRF, 3, A119, https://doi.org/10.17815/jlsrf-3-163, 2017.

Koop, T., Luo, B. P., Tsias, A., and Peter, T.: Water activity as the determinant for homogeneous ice nucleation in aqueous solutions, Nature, 406, 611–614, https://doi.org/10.1038/35020537, 2000.

Kulkarni, G., Sanders, C., Zhang, K., Liu, X., and Zhao, C.: Ice nucleation of bare and sulfuric acid-coated mineral dust particles and implication for cloud properties, Journal of Geophysical Research: Atmospheres, 119, 9993–10 011, https://doi.org/https://doi.org/10.1002/2014JD021567, 2014.

Kärcher, B. and Podglajen, A.: A Stochastic Representation of Temperature Fluctuations Induced by Mesoscale Gravity Waves, Journal of Geophysical Research: Atmospheres, 124, 11 506–11 529, https://doi.org/10.1029/2019JD030680, 2019.

Kärcher, B., Hendricks, J., and Lohmann, U.: Physically based parameterization of cirrus cloud formation for use in global atmospheric models, Journal of Geophysical Research: Atmospheres, 111, https://doi.org/10.1029/2005JD006219, 2006.

Law, K. S., Stohl, A., Quinn, P. K., Brock, C. A., Burkhart, J. F., Paris, J.-D., Ancellet, G., Singh, H. B., Roiger, A., Schlager, H., Dibb, J., Jacob, D. J., Arnold, S. R., Pelon, J., and Thomas, J. L.: Arctic Air Pollution: New Insights from POLARCAT-IPY, Bulletin of the American Meteorological Society, 95, 1873–1895, https://doi.org/10.1175/BAMS-D-13-00017.1, 2014.

Li, G., Wieder, J., Pasquier, J. T., Henneberger, J., and Kanji, Z. A.: Predicting atmospheric background number concentration of ice-nucleating particles in the Arctic, Atmospheric Chemistry and Physics, 22, 14 441–14 454, https://doi.org/10.5194/acp-22-14441-2022, 2022.

Mamouri, R.-E. and Ansmann, A.: Potential of polarization lidar to provide profiles of CCN- and INP-relevant aerosol parameters, Atmospheric Chemistry and Physics, 16, 5905–5931, https://doi.org/10.5194/acp-16-5905-2016, 2016.

Mamouri, R.-E. and Ansmann, A.: Potential of polarization/Raman lidar to separate fine dust, coarse dust, maritime, and anthropogenic aerosol profiles, Atmospheric Measurement Techniques, 10, 3403–3427, https://doi.org/10.5194/amt-10-3403-2017, 2017.

Mamouri, R.-E., Ansmann, A., Ohneiser, K., Knopf, D. A., Nisantzi, A., Bühl, J., Engelmann, R., Skupin, A., Seifert, P., Baars, H., Ene, D., Wandinger, U., and Hadjimitsis, D.: Wildfire smoke triggers cirrus formation: Lidar observations over the Eastern Mediterranean (Cyprus), EGUsphere, 2023, 1–30, https://doi.org/10.5194/egusphere-2023-988, 2023.

Marinou, E., Tesche, M., Nenes, A., Ansmann, A., Schrod, J., Mamali, D., Tsekeri, A., Pikridas, M., Baars, H., Engelmann, R., Voudouri, K.-A., Solomos, S., Sciare, J., Groß, S., Ewald, F., and Amiridis, V.: Retrieval of ice-nucleating particle concentrations from lidar observations and comparison with UAV in situ measurements, Atmospheric Chemistry and Physics, 19, 11 315–11 342, https://doi.org/10.5194/acp-19-11315-2019, 2019.

Martinsson, B. G., Friberg, J., Sandvik, O. S., Hermann, M., van Velthoven, P. F. J., and Zahn, A.: Formation and composition of the UTLS aerosol, npj Clim. Atmos. Sci., 2, https://doi.org/10.1038/s41612-019-0097-1, 2019.

Mason, S. L., Hogan, R. J., Bozzo, A., and Pounder, N. L.: A unified synergistic retrieval of clouds, aerosols, and precipitation from Earth-CARE: the ACM-CAP product, Atmospheric Measurement Techniques, 16, 3459–3486, https://doi.org/10.5194/amt-16-3459-2023, 2023.

Mattis, I., Ansmann, A., Müller, D., Wandinger, U., and Althausen, D.: Multiyear aerosol observations with dual-wavelength Raman lidar in the framework of EARLINET, Journal of Geophysical Research: Atmospheres, 109, https://doi.org/10.1029/2004JD004600, 2004.

Maturilli, M., Holdridge, D. J., Dahlke, S., Graeser, J., Sommerfeld, A., Jaiser, R., Deckelmann, H., and Schulz, A.: Initial radiosonde data from 2019-10 to 2020-09 during project MOSAiC, https://doi.org/10.1594/PANGAEA.928656, 2021.

Murray, B. J., Wilson, T. W., Dobbie, S., and Cui, Z.: Heterogeneous nucleation of ice particles on glassy aerosols under cirrus conditions, Nature Geoscience, 3, 233–237, https://doi.org/10.1038/ngeo817, 2010.

Möhler, O., Benz, S., Saathoff, H., Schnaiter, M., Wagner, R., Schneider, J., Walter, S., Ebert, V., and Wagner, S.: The effect of organic coating on the heterogeneous ice nucleation efficiency of mineral dust aerosols, Environmental Research Letters, 3, 1–8, https://doi.org/10.1088/1748-9326/3/2/025007, 2008.

Nixdorf, U., Dethloff, K., Rex, M., Shupe, M., Sommerfeld, A., Perovich, D., Nicolaus, M., Heuze´, C., Rabe, B., Loose, B., Damm, E., Gradinger, R., Fong., A, Maslowski, W., Rinke, A., Kwok, R., Spreen, G., Wendisch, M., Herber, A., Hirsekorn, M., Mohaupt, V., Frickenhaus, S., Immerz, A., Weiss-Tuider, K., König, B., Mengedoht, D., Regnery, J., Gerchow, P., Ransby, D., Krumpen, T., Morgenstern, A., Haas, C., Kanzow, T., Rack, F. R., Saitzev, V., Sokolov, V., Makarov, A., Schwarze, S., Wunderlich, T., Wurr, K., and Boetius, A.: MOSAiC extended acknowledgement, Zenodo, https://doi.org/10.5281/zenodo.5179738, 2021.

Ohneiser, K., Ansmann, A., Baars, H., Seifert, P., Barja, B., Jimenez, C., Radenz, M., Teisseire, A., Floutsi, A., Haarig, M., Foth, A., Chudnovsky, A., Engelmann, R., Zamorano, F., Bühl, J., and Wandinger, U.: Smoke of extreme Australian bushfires observed in the stratosphere over Punta Arenas, Chile, in January 2020: optical thickness, lidar ratios, and depolarization ratios at 355 and 532 nm, Atmospheric Chemistry and Physics, 20, 8003–8015, https://doi.org/10.5194/acp-20-8003-2020, 2020.

Ohneiser, K., Ansmann, A., Chudnovsky, A., Engelmann, R., Ritter, C., Veselovskii, I., Baars, H., Gebauer, H., Griesche, H., Radenz, M., Hofer, J., Althausen, D., Dahlke, S., and Maturilli, M.: The unexpected smoke layer in the High Arctic winter stratosphere during MOSAiC 2019–2020, Atmospheric Chemistry and Physics, 21, 15 783–15 808, https://doi.org/10.5194/acp-21-15783-2021, 2021.

Ohneiser, K., Ansmann, A., Kaifler, B., Chudnovsky, A., Barja, B., Knopf, D. A., Kaifler, N., Baars, H., Seifert, P., Villanueva, D., Jimenez, C., Radenz, M., Engelmann, R., Veselovskii, I., and Zamorano, F.: Australian wildfire smoke in the stratosphere: the decay phase in 2020/21 and impact on ozone depletion, Atmospheric Chemistry and Physics Discussions, 2022, 1–41, https://doi.org/10.5194/acp-2021-1097, 2022.

Ohneiser, K., Ansmann, A., Witthuhn, J., Deneke, H., Chudnovsky, A., Walter, G., and Senf, F.: Self-lofting of wildfire smoke in the troposphere and stratosphere: simulations and space lidar observations, Atmospheric Chemistry and Physics, 23, 2901–2925, https://doi.org/10.5194/acp-23-2901-2023, 2023.

O'Sullivan, D., Murray, B. J., Malkin, T. L., Whale, T. F., Umo, N. S., Atkinson, J. D., Price, H. C., Baustian, K. J., Browse, J., and Webb, M. E.: Ice nucation by fertile soil dusts: relative importance of mineral and biogenic components, Atmospheric Chemistry and Physics, 14, 1853–1867, https://doi.org/10.5194/acp-14-1853-2014, 2014.

Peng, S., Yang, Q., Shupe, M. D., Xi, X., Han, B., Chen, D., Dahlke, S., and Liu, C.: The characteristics of atmospheric boundary layer height over the Arctic Ocean during MOSAiC, Atmospheric Chemistry and Physics, 23, 8683–8703, https://doi.org/10.5194/acp-23-8683-2023, 2023.

Polly(2022): PollyNET lidar data base, available at: http://polly.tropos.de/, last access: 10 December, 2022.

Radenz, M., Seifert, P., Baars, H., Floutsi, A. A., Yin, Z., and Bühl, J.: Automated time–height-resolved air mass source attribution for profiling remote sensing applications, Atmospheric Chemistry and Physics, 21, 3015–3033, https://doi.org/10.5194/acp-21-3015-2021, 2021.

Ramelli, F., Henneberger, J., David, R. O., Bühl, J., Radenz, M., Seifert, P., Wieder, J., Lauber, A., Pasquier, J. T., Engelmann, R., Mignani, C., Hervo, M., and Lohmann, U.: Microphysical investigation of the seeder and feeder region of an Alpine mixed-phase cloud, Atmospheric Chemistry and Physics, 21, 6681–6706, https://doi.org/10.5194/acp-21-6681-2021, 2021.

Rigg, Y. J., Alpert, P. A., and Knopf, D. A.: Immersion freezing of water and aqueous ammonium sulfate droplets initiated by humic-like substances as a function of water activity, Atmospheric Chemistry and Physics, 13, 6603–6622, https://doi.org/10.5194/acp-13-6603-2013, 2013.

Rinke, A., Cassano, J. J., Cassano, E. N., Jaiser, R., and Handorf, D.: Meteorological conditions during the MOSAiC expedition: Normal or anomalous?, Elementa: Science of the Anthropocene, 9, https://doi.org/10.1525/elementa.2021.00023, 00023, 2021.

Ritter, C., Neuber, R., Schulz, A., Markowicz, K., Stachlewska, I., Lisok, J., Makuch, P., Pakszys, P., Markuszewski, P., Rozwadowska, A., Petelski, T., Zielinski, T., Becagli, S., Traversi, R., Udisti, R., and Gausa, M.: 2014 iAREA campaign on aerosol in Spitsbergen – Part 2: Optical properties from Raman-lidar and in-situ observations at Ny-Ålesund, Atmospheric Environment, 141, 1–19, https://doi.org/10.1016/j.atmosenv.2016.05.053, 2016.

Rolph, G., Stein, A., and Stunder, B.: Real-time Environmental Applications and Display sYstem: READY, Environmental Modelling & Software, 95, 210–228, https://doi.org/10.1016/j.envsoft.2017.06.025, 2017.

Schmale, J., Zieger, P., and Ekman, A.: Aerosols in current and future Arctic climate, Nat. Clim. Chang., 11, 95–105, https://doi.org/10.1038/s41558-020-00969-5, 2021.

Schmale, J., Sharma, S., Decesari, S., Pernov, J., Massling, A., Hansson, H.-C., von Salzen, K., Skov, H., Andrews, E., Quinn, P. K., Upchurch, L. M., Eleftheriadis, K., Traversi, R., Gilardoni, S., Mazzola, M., Laing, J., and Hopke, P.: Pan-Arctic seasonal cycles and long-term trends of aerosol properties from 10 observatories, Atmospheric Chemistry and Physics, 22, 3067–3096, https://doi.org/10.5194/acp-22-3067-2022, 2022.

Shupe, M. D., Walden, V. P., Eloranta, E., Uttal, T., Campbell, J. R., Starkweather, S. M., and Shiobara, M.: Clouds at Arctic Atmospheric Observatories. Part I: Occurrence and Macrophysical Properties, J. Appl. Meteorol. Clim., 50, 626–644, https://doi.org/10.1175/2010jamc2467.1, 2011.

Shupe, M. D., Rex, M., Blomquist, B., Ola, P., Persson, G., Schmale, J., Uttal, T., Althausen, D., Angot, H., Archer, S., Bariteau, L., Beck, I., Bilberry, J., Bucci, S., Buck, C., Boyer, M., Brasseur, Z., Brooks, I. M., Calmer, R., Cassano, J., Castro, V., Chu, D., Costa, D., Cox, C. J., Creamean, J., Crewell, S., Dahlke, S., Damm, E., de Boer, G., Deckelmann, H., Dethloff, K., Dütsch, M., Ebell, K., Ehrlich, A., Ellis, J., Engelmann, R., Fong, A. A., Frey, M. M., Gallagher, M. R., Ganzeveld, L., Gradinger, R., Graeser, J., Greenamyer, V., Griesche, H., Griffiths, S., Hamilton, J., Heinemann, G., Helmig, D., Herber, A., Heuzé, C., Hofer, J., Houchens, T., Howard, D., Inoue, J., Jacobi, H.-W., Jaiser, R., Jokinen, T., Jourdan, O., Jozef, G., King, W., Kirchgaessner, A., Klingebiel, M., Krassovski, M., Krumpen, T., Lampert, A., Landing, W., Laurila, T., Lawrence, D., Lonardi, M., Loose, B., Lüpkes, C., Maahn, M., Macke, A., Maslowski, W., Marsay, C., Maturilli, M., Mech, M., Morris, S., Moser, M., Nicolaus, M., Ortega, P., Osborn, J., Pätzold, F., Perovich, D. K., Petäjä, T., Pilz, C., Pirazzini, R., Posman, K., Powers, H., Pratt, K. A., Preußer, A., Quéléver, L., Radenz, M., Rabe, B., Rinke, A., Sachs, T., Schulz, A., Siebert, H., Silva, T., Solomon, A., Sommerfeld, A., Spreen, G., Stephens, M., Stohl, A., Svensson, G., Uin, J., Viegas, J., Voigt, C., von der Gathen, P., Wehner, B., Welker, J. M., Wendisch, M., Werner, M., Xie, Z., and Yue, F.: Overview of the MOSAiC expedition: Atmosphere, Elementa: Science of the Anthropocene, 10, https://doi.org/10.1525/elementa.2021.00060, 2022.

Si, M., Evoy, E., Yun, J., Xi, Y., Hanna, S. J., Chivulescu, A., Rawlings, K., Veber, D., Platt, A., Kunkel, D., Hoor, P., Sharma, S., Leaitch, W. R., and Bertram, A. K.: Concentrations, composition, and sources of ice-nucleating particles in the Canadian High Arctic during spring 2016, Atmospheric Chemistry and Physics, 19, 3007–3024, https://doi.org/10.5194/acp-19-3007-2019, 2019.

1135 Skupin, A., Ansmann, A., Engelmann, R., Seifert, P., and Müller, T.: Four-year long-path monitoring of ambient aerosol extinction at a central European urban site: dependence on relative humidity, Atmospheric Chemistry and Physics, 16, 1863–1876, https://doi.org/10.5194/acp-16-1863-2016, 2016.

Smirnov, A., Holben, B. N., Slutsker, I., Giles, D. M., McClain, C. R., Eck, T. F., Sakerin, S. M., Macke, A., Croot, P., Zibordi, G., Quinn, P. K., Sciare, J., Kinne, S., Harvey, M., Smyth, T. J., Piketh, S., Zielinski, T., Proshutinsky, A., Goes, J. I., Nelson, N. B., Larouche, P., Ra-

1140 dionov, V. F., Goloub, P., Krishna Moorthy, K., Matarrese, R., Robertson, E. J., and Jourdin, F.: Maritime Aerosol Network as a component of Aerosol Robotic Network, Journal of Geophysical Research: Atmospheres, 114, https://doi.org/https://doi.org/10.1029/2008JD011257, 2009.

Spichtinger, P. and Cziczo, D. J.: Impact of heterogeneous ice nuclei on homogeneous freezing events in cirrus clouds, Journal of Geophysical Research: Atmospheres, 115, https://doi.org/10.1029/2009JD012168, 2010.

1145 Spichtinger, P., Gierens, K., and Dörnbrack, A.: Formation of ice supersaturation by mesoscale gravity waves, Atmospheric Chemistry and Physics, 5, 1243–1255, https://doi.org/10.5194/acp-5-1243-2005, 2005.

Stein, A. F., Draxler, R. R., Rolph, G. D., Stunder, B. J. B., Cohen, M. D., and Ngan, F.: NOAA's HYSPLIT Atmospheric Transport and Dispersion Modeling System, Bulletin of the American Meteorological Society, 96, 2059–2077, https://doi.org/10.1175/BAMS-D-14-00110.1, 2015.

1150 Stephens, G., Vane, D., Boain, R., Mace, G., Sassen, K., Wang, Z., Illingworth, A., O'Connor, E., Rossow, W., Durden, S., Miller, S., Austin, R., Benedetti, A., and Mitrescu, C.: The CloudSat mission and the A-Train , Bulletin of the American Meteorological Society, 83, 1771–1790, https://doi.org/10.1175/BAMS-83-12-1771, 2002.

Stohl, A.: Characteristics of atmospheric transport into the Arctic troposphere, Journal of Geophysical Research: Atmospheres, 111, https://doi.org/10.1029/2005JD006888, 2006.

1155 Sze, K. C. H., Wex, H., Hartmann, M., Skov, H., Massling, A., Villanueva, D., and Stratmann, F.: Ice-nucleating particles in northern Greenland: annual cycles, biological contribution and parameterizations, Atmospheric Chemistry and Physics, 23, 4741–4761, https://doi.org/10.5194/acp-23-4741-2023, 2023.

Tatzelt, C., Henning, S., Welti, A., Baccarini, A., Hartmann, M., Gysel-Beer, M., van Pinxteren, M., Modini, R. L., Schmale, J., and Stratmann, F.: Circum-Antarctic abundance and properties of CCN and INPs, Atmospheric Chemistry and Physics, 22, 9721–9745,

1160 https://doi.org/10.5194/acp-22-9721-2022, 2022.

Tobo, Y., DeMott, P. J., Hill, T. C. J., Prenni, A. J., Swoboda-Colberg, N. G., Franc, G. D., and Kreidenweis, S. M.: Organic matter matters for ice nuclei of agricultural soil origin, Atmospheric Chemistry and Physics, 14, 8521–8531, https://doi.org/10.5194/acp-14-8521-2014, 2014.

Tobo, Y., Adachi, K., DeMott, P. J., Hill, T. C. J., Hamilton, D. S., Mahowald, N. M., Nagatsuka, N., Ohata, S., Uetake, J., Kondo, Y.,

1165 and Koike, M.: Glacially sourced dust as a potentially significant source of ice nucleating particles, Nature Geoscience, 12, 253–258, https://doi.org/10.1038/s41561-019-0314-x, 2019.

Tomasi, C., Lupi, A., Mazzola, M., Stone, R. S., Dutton, E. G., Herber, A., Radionov, V. F., Holben, B. N., Sorokin, M. G., Sakerin, S. M., Terpugova, S. A., Sobolewski, P. S., Lanconelli, C., Petkov, B. H., Busetto, M., and Vitale, V.: An update on polar aerosol optical properties using POLAR-AOD and other measurements performed during the International Polar Year, Atmospheric Environment, 52, 29–

47, https://doi.org/https://doi.org/10.1016/j.atmosenv.2012.02.055, physical, chemical, optical and radiative properties of polar aerosols – IPY 2007 - 2008, 2012.

Tomasi, C., Kokhanovsky, A. A., Lupi, A., Ritter, C., Smirnov, A., O'Neill, N. T., Stone, R. S., Holben, B. N., Nyeki, S., Wehrli, C., Stohl, A., Mazzola, M., Lanconelli, C., Vitale, V., Stebel, K., Aaltonen, V., de Leeuw, G., Rodriguez, E., Herber, A. B., Radionov, V. F., Zielinski, T., Petelski, T., Sakerin, S. M., Kabanov, D. M., Xue, Y., Mei, L., Istomina, L., Wagener, R., McArthur, B., Sobolewski, P. S., Kivi, R., Courcoux, Y., Larouche, P., Broccardo, S., and Piketh, S. J.: Aerosol remote sensing in polar regions, Earth-Science Reviews, 140, 108–157, https://doi.org/10.1016/j.earscirev.2014.11.001, 2015.

Torres, O., Jethva, H., Ahn, C., Jaross, G., and Loyola, D. G.: TROPOMI aerosol products: evaluation and observations of synoptic-scale carbonaceous aerosol plumes during 2018–2020, Atmospheric Measurement Techniques, 13, 6789–6806, https://doi.org/10.5194/amt-13-6789-2020, 2020.

Toth, T. D., Campbell, J. R., Reid, J. S., Tackett, J. L., Vaughan, M. A., Zhang, J., and Marquis, J. W.: Minimum aerosol layer detection sensitivities and their subsequent impacts on aerosol optical thickness retrievals in CALIPSO level 2 data products, Atmospheric Measurement Techniques, 11, 499–514, https://doi.org/10.5194/amt-11-499-2018, 2018.

Ullrich, R., Hoose, C., Möhler, O., Niemand, M., Wagner, R., Höhler, K., Hiranuma, N., Saathoff, H., and Leisner, T.: A New Ice Nucleation Active Site Parameterization for Desert Dust and Soot, Journal of the Atmospheric Sciences, 74, 699–717, https://doi.org/10.1175/JAS-D-16-0074.1, 2017.

Wang, B. and Knopf, D. A.: Heterogeneous ice nucleation on particles composed of humic-like substances impacted by O_3, Journal of Geophysical Research: Atmospheres, 116, https://doi.org/10.1029/2010JD014964, 2011.

Wang, B., Lambe, A. T., Massoli, P., Onasch, T. B., Davidovits, P., Worsnop, D. R., and Knopf, D. A.: The deposition ice nucleation and immersion freezing potential of amorphous secondary organic aerosol: Pathways for ice and mixed-phase cloud formation, Journal of Geophysical Research: Atmospheres, 117, https://doi.org/https://doi.org/10.1029/2012JD018063, 2012.

Wang, Q., Jacob, D. J., Fisher, J. A., Mao, J., Leibensperger, E. M., Carouge, C. C., Le Sager, P., Kondo, Y., Jimenez, J. L., Cubison, M. J., and Doherty, S. J.: Sources of carbonaceous aerosols and deposited black carbon in the Arctic in winter-spring: implications for radiative forcing, Atmospheric Chemistry and Physics, 11, 12 453–12 473, https://doi.org/10.5194/acp-11-12453-2011, 2011.

Westbrook, C. D. and Illingworth, A. J.: Evidence that ice forms primarily in supercooled liquid clouds at temperatures > -27°C, Geophysical Research Letters, 38, https://doi.org/10.1029/2011GL048021, 2011.

Wex, H., DeMott, P. J., Tobo, Y., Hartmann, S., Rösch, M., Clauss, T., Tomsche, L., Niedermeier, D., and Stratmann, F.: Kaolinite particles as ice nuclei: learning from the use of different kaolinite samples and different coatings, Atmospheric Chemistry and Physics, 14, 5529–5546, https://doi.org/10.5194/acp-14-5529-2014, 2014.

Wex, H., Huang, L., Zhang, W., Hung, H., Traversi, R., Becagli, S., Sheesley, R. J., Moffett, C. E., Barrett, T. E., Bossi, R., Skov, H., Hünerbein, A., Lubitz, J., Löffler, M., Linke, O., Hartmann, M., Herenz, P., and Stratmann, F.: Annual variability of ice-nucleating particle concentrations at different Arctic locations, Atmospheric Chemistry and Physics, 19, 5293–5311, https://doi.org/10.5194/acp-19-5293-2019, 2019.

Willis, M. D., Leaitch, W. R., and Abbatt, J. P.: Processes controlling the composition and abundance of Arctic aerosol, Reviews of Geophysics, 56, 621–671, https://doi.org/10.1029/2018RG000602, 2018.

Willis, M. D., Bozem, H., Kunkel, D., Lee, A. K. Y., Schulz, H., Burkart, J., Aliabadi, A. A., Herber, A. B., Leaitch, W. R., and Abbatt, J. P. D.: Aircraft-based measurements of High Arctic springtime aerosol show evidence for vertically varying sources, transport and composition, Atmospheric Chemistry and Physics, 19, 57–76, https://doi.org/10.5194/acp-19-57-2019, 2019.

Winker, D. M., Vaughan, M. A., Omar, A., Hu, Y., Powell, K. A., Liu, Z., Hunt, W. H., and Young, S. A.: Overview of the CALIPSO mission and CALIOP data processing algorithms, Journal of Atmospheric and Oceanic Technology, 26, 2310–2323, https://doi.org/10.1175/2009JTECHA1281.1, 2009.

Winker, D. M., Pelon, J., Coakley, J. A., Ackerman, S. A., Charlson, R. J., Colarco, P. R., Flamant, P. H., Fu, Q., Hoff, R. M., Kittaka, C., Kubar, T. L., Treut, H. L., McCormick, M. P., Mégie, G., Poole, L. R., Powell, K., Trepte, C. R., Vaughan, M. A., and Wielicki, B. A.: The CALIPSO mission: A global 3D view of aerosols and clouds, Bulletin of the American Meteorological Society, 91, 1211–1229, 2010.

Xian, P., Zhang, J., O'Neill, N. T., Toth, T. D., Sorenson, B., Colarco, P. R., Kipling, Z., Hyer, E. J., Campbell, J. R., Reid, J. S., and Ranjbar, K.: Arctic spring and summertime aerosol optical depth baseline from long-term observations and model reanalyses – Part 1: Climatology and trend, Atmospheric Chemistry and Physics, 22, 9915–9947, https://doi.org/10.5194/acp-22-9915-2022, 2022a.

Xian, P., Zhang, J., O'Neill, N. T., Reid, J. S., Toth, T. D., Sorenson, B., Hyer, E. J., Campbell, J. R., and Ranjbar, K.: Arctic spring and summertime aerosol optical depth baseline from long-term observations and model reanalyses – Part 2: Statistics of extreme AOD events, and implications for the impact of regional biomass burning processes, Atmospheric Chemistry and Physics, 22, 9949–9967, https://doi.org/10.5194/acp-22-9949-2022, 2022b.

Yang, Y., Zhao, C., Wang, Q., Cong, Z., Yang, X., and Fan, H.: Aerosol characteristics at the three poles of the Earth as characterized by Cloud–Aerosol Lidar and Infrared Pathfinder Satellite Observations, Atmospheric Chemistry and Physics, 21, 4849–4868, https://doi.org/10.5194/acp-21-4849-2021, 2021.

Yin, Z., Ansmann, A., Baars, H., Seifert, P., Engelmann, R., Radenz, M., Jimenez, C., Herzog, A., Ohneiser, K., Hanbuch, K., Blarel, L., Goloub, P., Dubois, G., Victori, S., and Maupin, F.: Aerosol measurements with a shipborne Sun–sky–lunar photometer and collocated multiwavelength Raman polarization lidar over the Atlantic Ocean, Atmospheric Measurement Techniques, 12, 5685–5698, https://doi.org/10.5194/amt-12-5685-2019, 2019.

Yu, P., Toon, O. B., Bardeen, C. G., Zhu, Y., Rosenlof, K. H., Portmann, R. W., Thornberry, T. D., Gao, R.-S., Davis, S. M., Wolf, E. T., de Gouw, J., Peterson, D. A., Fromm, M. D., and Robock, A.: Black carbon lofts wildfire smoke high into the stratosphere to form a persistent plume, Science, 365, 587–590, https://doi.org/10.1126/science.aax1748, 2019.

Zeppenfeld, S., van Pinxteren, M., Hartmann, M., Bracher, A., Stratmann, F., and Herrmann, H.: Glucose as a Potential Chemical Marker for Ice Nucleating Activity in Arctic Seawater and Melt Pond Samples, Environmental Science & Technology, 53, 8747–8756, https://doi.org/10.1021/acs.est.9b01469, pMID: 31248257, 2019.

Zhao, X., Huang, K., Fu, J. S., and Abdullaev, S. F.: Long-range transport of Asian dust to the Arctic: identification of transport pathways, evolution of aerosol optical properties, and impact assessment on surface albedo changes, Atmospheric Chemistry and Physics, 22, 10 389–10 407, https://doi.org/10.5194/acp-22-10389-2022, 2022.

Table 1. Overview of Polly observational products, used in this study, and typical relative uncertainties in the determined and retrieved properties. Particle backscatter coefficients are measured at 355, 532, and 1064 nm, the other aerosol optical properties at 355 and 532 nm. r denotes aerosol particle radius.

Aerosol optical properties	Uncertainty
Backscatter coef. $[\mathrm{Mm}^{-1}\,\mathrm{sr}^{-1}]$	$\leq 10\%$
Extinction coefficient $[\mathrm{Mm}^{-1}]$	20%
Lidar ratio [sr]	25%
Depolarization ratio	$\leq 10\%$
Aerosol microphysical properties	
Volume conc. $[\mu\mathrm{g}\,\mathrm{m}^{-3}]$	$\leq 25\%$
Surface-area conc. $[\mu\mathrm{m}^2\,\mathrm{cm}^{-3}]$	$\leq 25\%$
Number conc. ($r > 85$ nm) $[\mathrm{cm}^{-3}]$	50%
Number conc. ($r > 290$ nm) $[\mathrm{cm}^{-3}]$	$\leq 25\%$
Cloud-relevant properties	
CCN conc. $[\mathrm{cm}^{-3}]$	50%
INP conc. $[\mathrm{L}^{-1}]$	Order of magn.

Table 2. Conversion parameters for Arctic aerosol, required in the conversion of the particle extinction coefficient σ at 532 nm into particle number concentrations n_{65}, n_{85}, n_{250}, and n_{290}, surface area concentration s, and volume concentration v. The mean values and range of mean values (from the 4 stations) for the conversion factors c_v, c_s, c_{65}, c_{85}, c_{250}, and c_{290} are obtained from the extended AERONET data analysis (AERONET, 2022). The conversion factors are derived from the AERONET observations at Barrow (1997-2021), Thule (2007-2021), Pearl (2007-2019), and Kangerlussuaq (2008-2021). All conversion factors hold for 532 nm wavelength. The AERONET data analysis procedures applied to obtain the conversion factors are described in Mamouri and Ansmann (2016, 2017).

Conversion factor	Value	Range of values
c_v $[10^{-12}\,\mathrm{Mm}]$	0.215	0.19-0.24
c_s $[10^{-12}\,\mathrm{Mm}\,\mathrm{m}^2\,\mathrm{cm}^{-3}]$	2.8	2.65-2.90
c_{65} $[\mathrm{Mm}\,\mathrm{cm}^{-3}]$	12.5	11.2-15.0
c_{85} $[\mathrm{Mm}\,\mathrm{cm}^{-3}]$	10.0	9.6-12.2
c_{250} $[\mathrm{Mm}\,\mathrm{cm}^{-3}]$	0.25	0.22-0.28
c_{290} $[\mathrm{Mm}\,\mathrm{cm}^{-3}]$	0.13	0.12-0.145
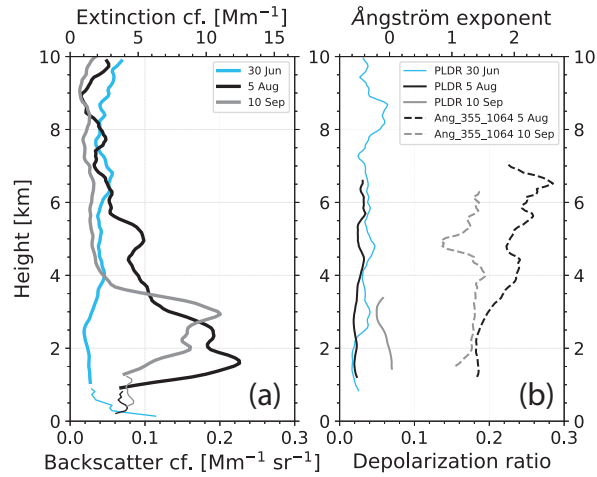
Figure 1. Pollution long-range transport towards the central Arctic at heights above 1 km observed with the Polarstern lidar on 5 August 2020 (lidar observations are averaged from 21:00-24:00 UTC, Polarstern position: 78.4°N, 6.0°W) and on 10 September 2020 (signal averaging from 18:15-21:10 UTC, Polarstern position: 88.7°N, 105.6°E). The measurement on 30 June 2020 shows clean background conditions (18:00-24:00 UTC, Polarstern at 81.8°N, 9.5°E). Backscatter and extinction profile segments from lidar observations with the near-range telescope are shown as thin solid lines up to about 1 km height in (a). The 532 nm extinction coefficients are obtained by multiplying the backscatter coefficients with a lidar ratio of 55 sr. In (b), the particle linear depolarization ratio (PLDR) at 532 nm for all three days and the backscatter-related Ångström exponent (Ang, considering the backscatter coefficients at 355 and 1064 nm) for the two pollution events on 5 August and 10 September2020 are given. The Ångström exponent was 1.5-2.0 throughout the troposphere during the clean background conditions on 30 June (not shown).
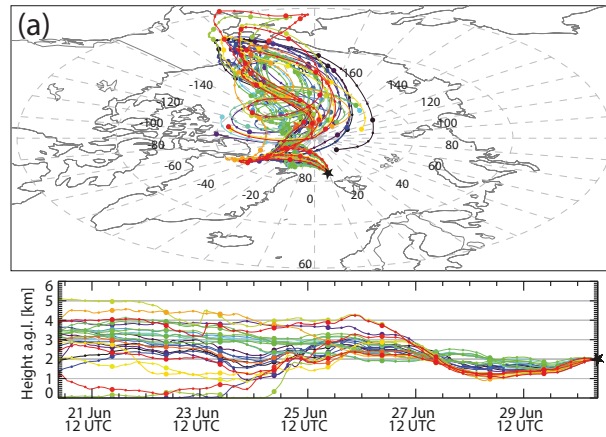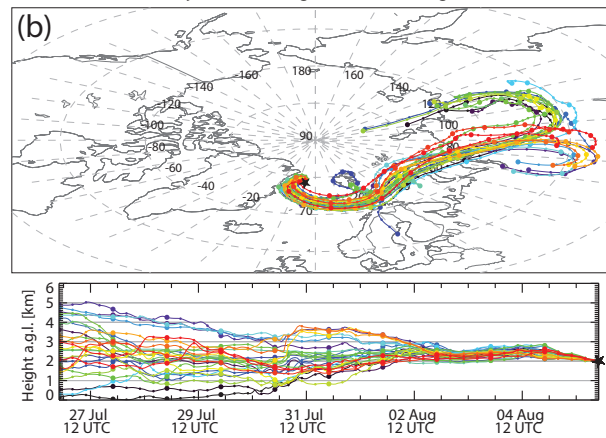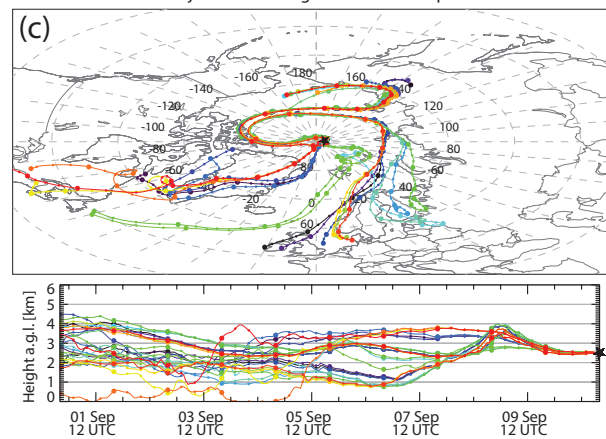
Figure 2. (a) HYSPLIT 10 d ensemble backward trajectories arriving over the Polarstern (indicated by a star) on (a) 30 June 2020, 21:00 UTC, (b) 5 August 2020, 22:00 UTC, and on (c) 10 September 2020, 21:00 UTC.
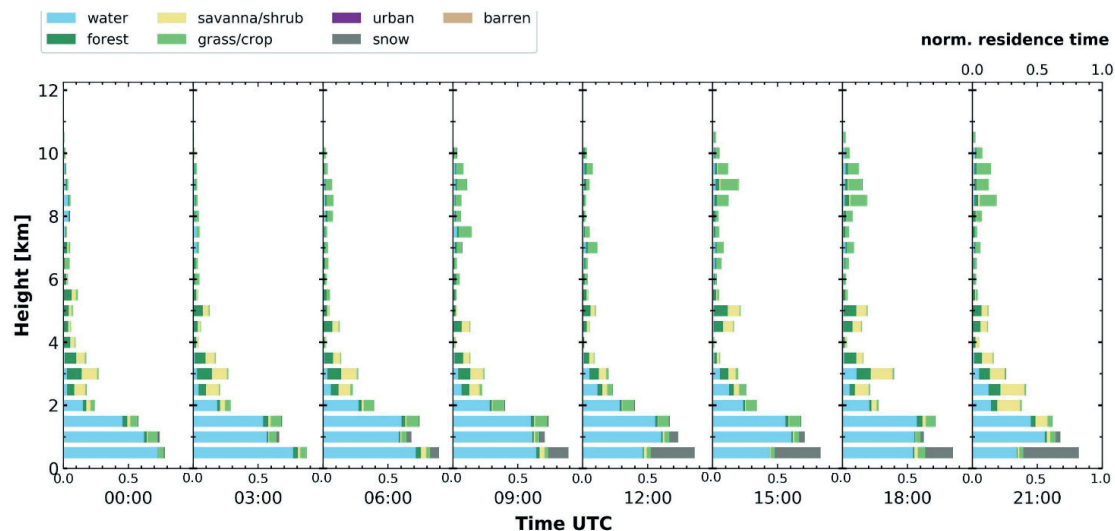
Figure 3. Vertically resolved air mass source attribution in 3 h intervals on 5 August 2020. The method of Radenz et al. (2021) is applied. The normalized (accumulated) residence time of air masses, when they traveled within the well-mixed boundary layer at heights below 2 km during the long-range transport, is given. The analysis is based on 10 d HYSPLIT backward trajectories arriving over Polarstern. The colors indicate different land cover classes. Continental particles contributed significantly to the backscatter and extinction coefficients, measured at heights >1 km on 5 August 2020, 18:00 and 21:00 UTC, shown in Fig. 1a.
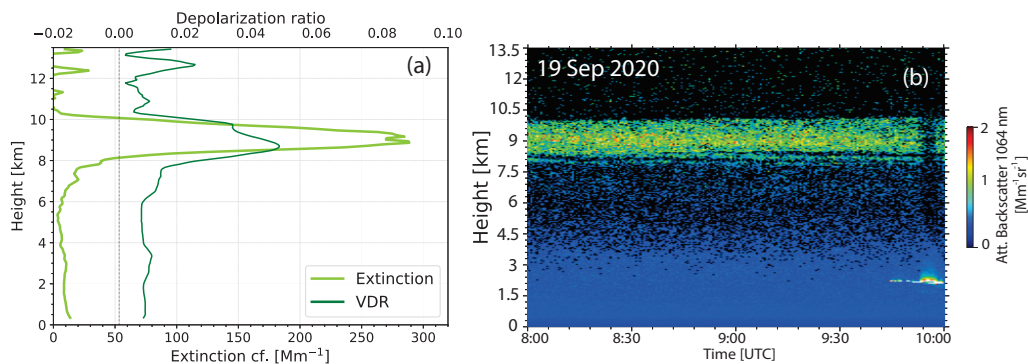
Figure 4. Wildfire smoke observed over Polarstern between 8 and 10 km height on 19 September 2020 (8:00-10:00 UTC, 89.1°N, 110°E). The smoke was probably lofted by strong convection over the western Pacific, west of California. Profiles of the 532 nm particle extinction coefficient (backscatter coefficient multiplied with a smoke lidar ratio of 70 sr) and the volume depolarization ratio (VDR) are shown in (a). Mean profiles for the time period from 8:00-9:40 UTC are presented. In (b), the height-time display of the 1064 nm range-corrected signal (or attenuated backscatter coefficient), showing the 2 km thick smoke layer, is given. The enhanced volume depolarization ratio of 5% is indicative for non-spherical smoke particles. The 532 nm AOT of the smoke layer was about 0.4.
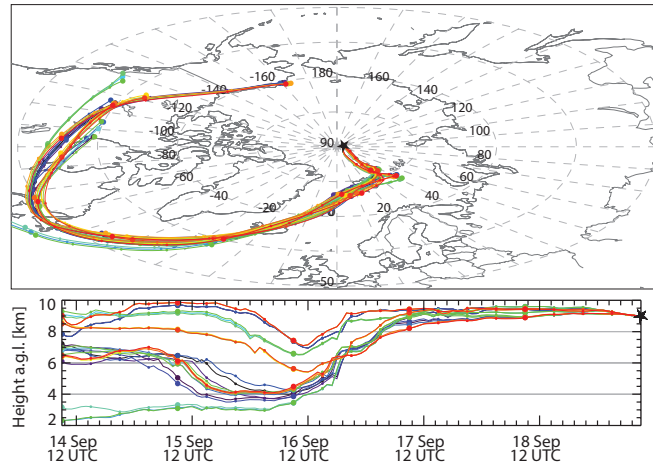
Figure 5. HYSPLIT 5 d ensemble backward trajectories arriving over the Polarstern (indicated by a star) on 19 September 2020, 09:00 UTC.
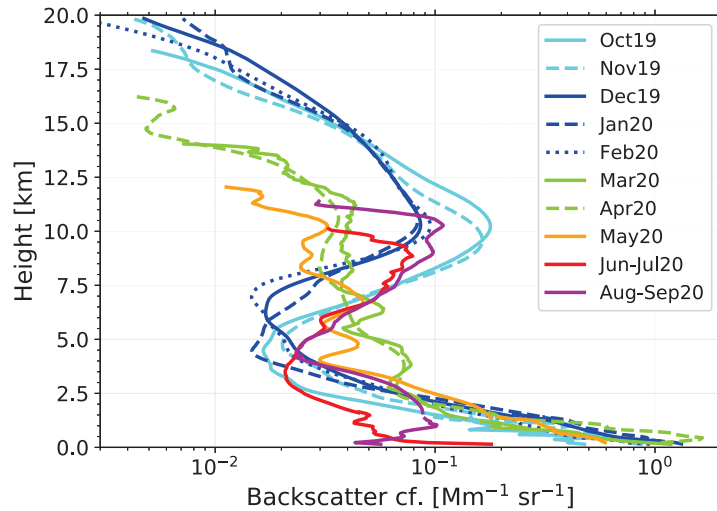
Figure 6. Aerosol layering over the central Arctic in 2019-2020. One-month and two-month mean particle backscatter profiles, measured at 532 nm, are shown. The UTLS height range (above 7.5 km) was strongly polluted by wildfire smoke (85% contribution to the particle backscatter coefficient) and Raikoke volcanic aerosol (15% backscatter fraction) during the autumn and winter months from October 2019 - Februray 2020 (cyan and blue colors).
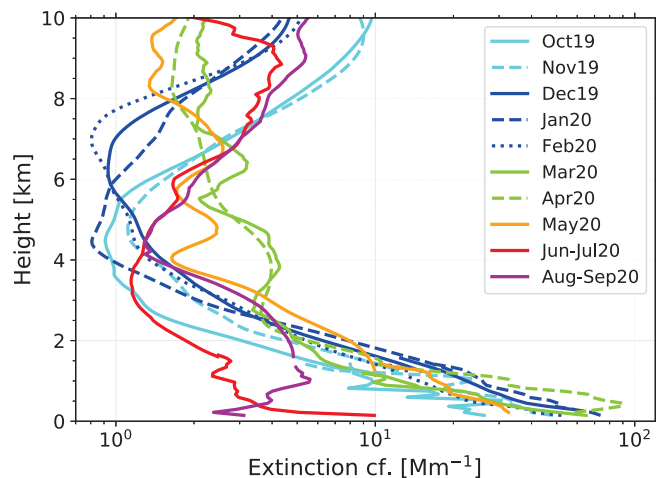
Figure 7. Tropospheric aerosol layering in terms of 1-month and 2-month mean particle light-extinction profiles (532 nm backsatter profiles shown in Fig. 6 times a lidar ratio of 55 sr). By combining lidar observations with the near-range telescope (covering the height range from 50-100 m up to 1.0-1.5 km) and the far-range telescope (covering the height range >1 km), particle extinction coefficients for the entire vertical tropospheric column could be determined. Continental aerosol pollution, soil dust, and biomass burning smoke dominated the aerosol conditions in the lowest 5 km, While wildfire smoke caused the re-increase of the extinction values at heights >5 km, especially from October 2019 - February 2020 and in September 2020.
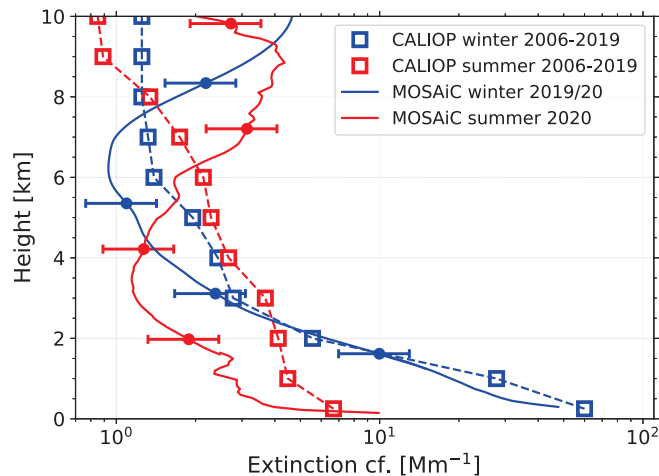
Figure 8. CALIOP (2006-2019) vs. MOSAiC (2019-2020) seasonal mean particle extinction profiles (532 nm) for the winter season (December-February) and summer season (June-August). CALIOP profiles are taken from Fig. 6 in Yang et al. (2021) and normalized with AOT shown in Fig. 3 in Yang et al. (2021). All CALIOP observations performed at latitudes between 65° and 82°N are considered. The MOSAiC extinction profiles are computed from the 532 nm backscatter profiles (multiplied with a lidar ratio of 55 sr). A few SD bars are given in the case of the MOSAiC observations.
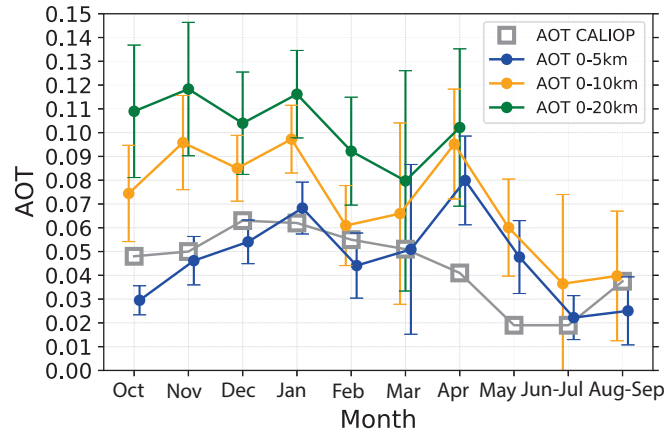
Figure 9. One-month and two-month mean AOTs for different height ranges measured during the MOSAiC expedition (October 2019 to September 2020). Backscatter profiles (532 nm) were multiplied with a typical tropospheric lidar ratio of 55 sr (0-5 km height) and a smoke lidar ratio of 85 sr (5-20 km) before the AOTs were computed. CALIOP AOT values (2006-2019 monthly means, 65-82°N mean, 0-12 km height range) are from Fig. 3. in Yang et al. (2021). SD bars are given in the case of the MOSAiC observations. For comparison, the MOSAiC MICROTOPS II sunphotometer observations revealed mean 500 nm AOTs of 0.055±0.014 (June-July) and 0.051±0.014 (August-September).
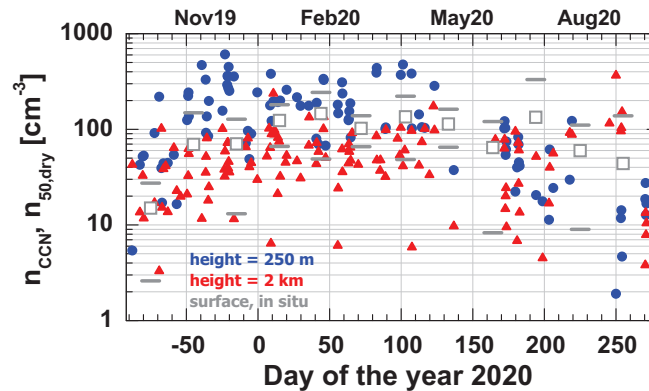
Figure 10. Annual cycle of the CCN number concentration (0.2% supersaturation) during the MOSAiC year, estimated from Polarstern lidar observations at 250 m (blue circles) and 2000 m height (red triangles) and observed in situ aboard Polarstern (gray squares, monthly mean CCN values, SD indicated by short gray horizontal bars, a few of the lower SD bars are <1 and thus not shown) (Boyer et al., 2023). Only $n_{CCN} < 700$ cm^{-3} (for the 250 m height level) are considered, corresponding to lidar-derived particle extinction coefficients <55 Mm^{-1} (indicating fog-free and cloudfree conditions).
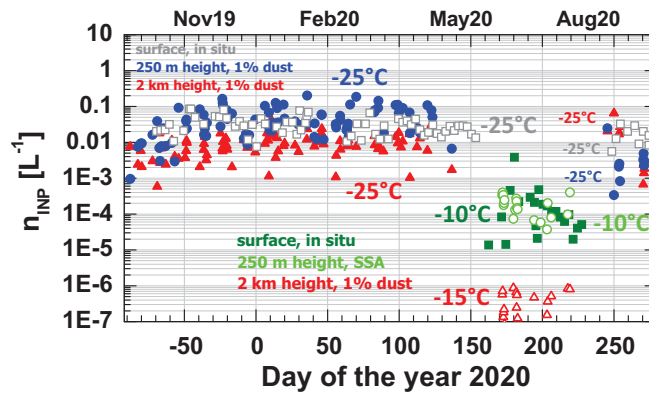
Figure 11. Annual cycle of the INP number concentration during the MOSAiC year as observed in situ aboard Polarstern (open gray and closed dark green squares, daily mean INP values) (Creamean et al., 2022) and estimated from Polarstern lidar observations at 250 m (closed blue circles, October 2019 - May 2020 and in September 2020, open light green circles from June-August) and at 2000 m height (closed red triangles, October - May and in September, red triangles from June-August) for ice-nucleating temperatures of $-25°C$ in autumn, winter, and spring and $-10°C$ (surface, 250 m) and $-15°C$ (2000 m) in summer. Clay mineral dust (1% contribution to the aerosol surface area concentration) is assumed to be the only ice-active aerosol type at 250 m (in autumn, winter, and spring) and 2000 m height (all seasons), while sea spray aerosol is assumed to be the only INP type at 250 m height in summer.
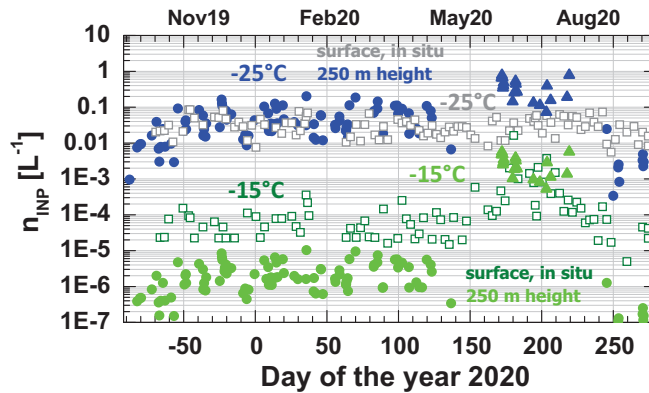
Figure 12. Same as Fig. 11, except for fixed temperatures of $-25°C$ (closed blue circles and open gray squares) and $-15°C$ (closed green circles and open green squares) throughout the MOSAiC year. Surface in situ observations (squares) (Creamean et al., 2022) and lidar INP estimates (circles for kaolinite dust, triangles for SSA) for the 250 m height level are shown.
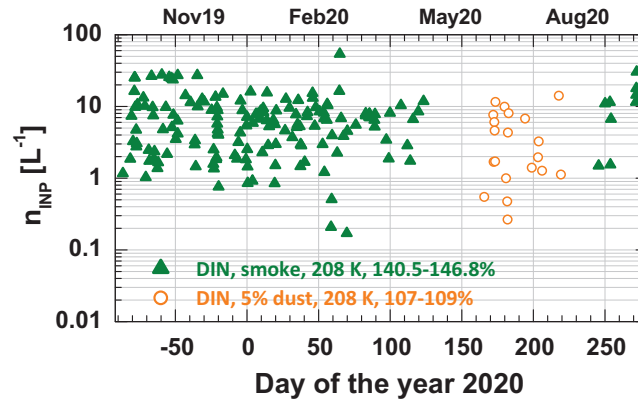
Figure 13. Lidar-estimated number concentrations of INPs, that would be available for the nucleation of ice crystals during a gravity-wave-induced updraft event of 35 s (dust INPs, open orange circles, June to August 2020, 5% dust fraction, aging factor $f_{\mathrm{age}} = 0.2$) and 88 s (smoke INPs, green triangles, autumn, winter, spring). The DIN time period of 35 and 88 s starts after exceeding $\mathrm{RH}_{\mathrm{ICE,on}}$ of 107% (dust) and 140.5% (smoke) and was (arbitrarily) terminated when $\mathrm{RH}_{\mathrm{ICE}}$ reached 109% (dust) and 146.8% (smoke) for temperatures close to 208 K. The variability in the INP values is directly linked to the lidar-estimated particle surface area concentration s_{dry}. The figure suggest that the aerosol concentration in the upper troposphere during the MOSAiC year was high enough to trigger cirrus formation via heterogeneous ice nucleation on smoke and dust INPs. The INP results are in line with retrievals of the ice crystal number concentration (0.1-10 L^{-1}) obtained from our MOSAiC radar-lidar-based data analysis.
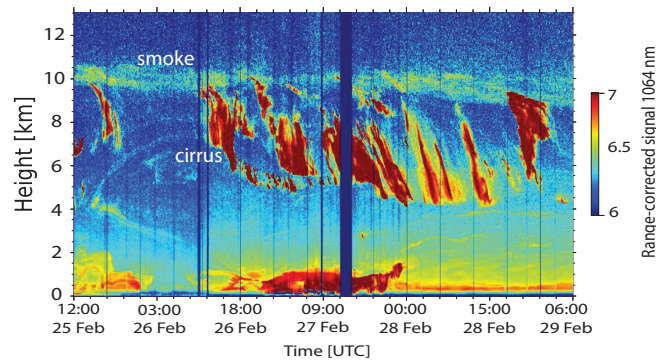
Figure 14. Lidar observations of cirrus formation in a wildfire smoke layer (in yellow around 10 km) on 25-29 February 2020. Coherent fall strikes (virga in orange and red) consisting of fastly growing, falling ice crystals developed quickly after nucleation of ice crystals in the smoke layer. The virga reached down to almost 4 km where the crystals evaporated in dry air. Temperatures were close to $-70°C$ at cirrus formation level. The range-corrected 1064 nm lidar return signal is shown in logarithmic scales (arbitray units).